Development of a Hybrid E-ΔE Detector to be used at DRAGON

Development of a Hybrid Ionization Chamber/Double-Sided-Silicon-Strip Detector to be Installed at the DRAGON Laboratory at TRIUMF

By

Devin Steward Maxwell Burke, B.Sc

A Thesis

Submitted to the School of Graduate Studies

in Partial Fulfilment of the Requirements

for the Degree

Master of Science

McMaster University

Master of Science (2016) McMaster University

(Department of Physics and Astronomy) Hamilton, Ontario

TITLE: Development of a Hybrid Ionization Chamber/Double-Sided-Silicon-Strip Detector to be Installed at the DRAGON Laboratory at TRIUMF

AUTHOR: Devin Burke, B.Sc

SUPERVISOR: Professor A. Chen

NUMBER OF PAGES: xiii, 83

Abstract

As of writing this thesis there are two detectors at TRIUMF's DRAGON facility which directly measure the kinetic energy (E) of heavy ions at the focal plane of its recoil separator. These are an ionization chamber and a double-sided-silicon-strip detector (DSSSD). The ionization chamber has inferior resolution to the DSSSD but can discriminate isobaric contaminants in a E-ΔE spectrum. A DSSSD has superior energy resolution and timing but cannot discriminate isobaric contaminants in many cases. A hybrid ionization chamber / double-sided-silicon-strip detector has been designed using the GEANT4 simulation package that combines the strengths of both these detector types. This hybrid detector design consists of an ionization chamber set in front of a DSSSD positioned at the end of the beamline of the recoil separator. The design presented here is specific to DRAGON's needs but can conceivably be re-purposed in other environments requiring heavy ion detection and identification and may be useful in fields such as health physics.

Acknowledgements

I would like to thank everybody that helped me throughout my master's studies at McMaster University and all my friends there who have supported me these last two years.

I would like to thank my supervisor Alan Chen for being a source of guidance and knowledge throughout the course of my master's education and for challenging me with this project. Thank you for always listening to my ideas and for encouraging me to pursue them.

Thank you to the entire DRAGON collaboration for all the conversations we had about the DRAGON facility and for just being great in general. I would especially like to thank Chris Ruiz who was my go to contact at DRAGON and who hosted my stay there for a summer to work on my detector and to participate in experiments.

I would also like to thank Dario Gigliotti who started this project and provided the first version of the GEANT4 application code used here.

Finally I would like to thank my parents for their love and encouragement and all the teachers I have ever had who helped me get here. It is only because of their support over the years that I have gotten this far.

~D.S Burke

Table of Contents

List of Figures

Chapter 1

Introduction

> We're made of star stuff. We are a way for the cosmos to know itself.
>
> Carl Sagan, Cosmos

The elements of the periodic table are the building blocks of all matter in the universe. The lightest of these were created at the birth of our universe, other elements were formed within the first stars which, like great cosmic furnaces, forged heavier elements and blasted them into space in their death throes. Their remains formed new stars, repeating the process to create all the elements we see around us. We are all made of star stuff. We are a brief coalescence of cosmic dust that has found a way to look at itself and wonder how it came to be.

Once thought indivisible it is now known that elements are themselves composed of protons, neutrons and electrons. The questions Nuclear Astrophysicists want to answer is how did all the elements and isotopes we see

around us come to be and how did all those protons, neutrons and electrons combine to form the elements and give form to the universe?

1.1 Nucleosynthesis

Nucleosynthesis is a family of nuclear reaction processes that result in the formation of heavy elements from lighter ones. In nature nucleosynthesis takes place in several different environments. Light nuclei up to $A = 7$ were formed shortly after the Big Bang in a process called Big Bang Nucleosynthesis. Nuclei from $A = 7 \sim 60$ were formed from stellar nucleosynthesis processes in stars such as the triple alpha process and C/O burning. Nuclei heavier than Fe were formed in asymptotic giant branch stars and the explosive environments of novae and x-ray bursters. In the following sections I will discuss the production of light nuclei ($A = 1 \sim 7$) shortly after the Big Bang, intermediate mass nuclei ($A = 7 \sim 60$) as the result of stellar fusion processes and heavy nuclei ($A > 60$) produced in explosive high energy environments.

1.1.1 Big Bang Nucleosynthesis

In the 1940's, George Gamow and associates claimed that the observed elemental abundances in the universe could be explained by nucleosynthesis reactions occurring within the first few minutes after the Big Bang [16]. Very soon after the big bang the universe underwent a period of exponential expansion and rapid cooling consisting of a soup of elementary particles. The universe continued to expand and cool. Once the universe cooled to a tem-

perature of 7.5×10^9 K high energy particles decayed to form protons and neutrons. When the universe cooled to 10^9 K, $p(n,\gamma)D$ reactions occurred and D nuclei were able to survive disruption by high energy photons. As the universe continued to cool, ^{3}He, ^{4}He, and T abundances were populated by reactions between D, p, n and product nuclei. Some small amounts of ^{7}Li were produced by T(^{4}He,γ)^{7}Li. Very small amounts of ^{7}Be were produced by ^{3}He(^{4}He,γ)^{7}Be but quickly decayed to ^{7}Li. Once temperatures dropped well below 10^9 K the light nuclei did not have enough thermal energy to overcome the coulomb barrier and nucleosynthesis ceased. These processes all occurred within the first five minutes of the lifetime of the universe. Gamow and associates were only correct in their claim for light nuclei up until ^{7}Li as indeed Big Bang Nucleosynthesis accounts for the majority of light elemental abundances in the universe. To account for elements heavier than lithium an improved theory was needed that included stellar fusion processes and synthesis in explosive environments [2].

1.1.2 Stellar Nucleosynthesis

Main sequence stars up to 1.3 $M_\odot$ fuse H into He, burning H as fuel in the well known p-p chain reaction. In stars larger than 1.3 $M_\odot$ He is also produced by the CNO cycle through catalytic reactions using C, N, and O as catalysts. Since C, N and O were not present in the early universe in the era of primordial stars, the CNO cycle could not have been present. Once a stellar core's supply of H is exhausted temperatures rise setting off He burning reactions which produce C and O and a small amount of Ne. C and O can

react to form Na, Mg, Al, Si, S and Ca. Beyond these reactions, at even higher temperatures the common metals Fe, Ni, Cr, Mn and Co are produced. Other elements not included here are produced in small secondary reactions in the hot stellar environment but in smaller amounts. If we follow the evolution of a single high mass star, we begin with the contraction of a nebular cloud to the formation of a protostar. Once the protostar reaches temperatures high enough for H to fuse it begins to burn H in the P-P chain or CNO cycle to form He. At this point it is considered a main sequence star. Once H is exhausted it will expand into a red giant and burn He. Once He is exhausted the core undergoes C/O burning and expands into a super giant. In this state it burns heavy elements up to Fe. Once it reaches Fe the binding energy per nucleon of any subsequent nuclear reactions to heavier nuclei are energetically unfavourable. With the star's fuel exhausted it will explode as a core-collapse supernova in which nucleosynthesis beyond Fe can occur. During a supernova layers of a star can also undergo explosive burning. The shock wave moving outwards from a star's core during a supernova will compress the shell structure of the ashes of previous burning processes triggering burning of each layer [2].

1.1.3 Nucleosynthesis beyond Fe

Nuclear fusion reactions above the Iron peak at A=56 are energetically unfavourable as the binding energy per nucleon decreases beyond the Fe peak. Burning above Fe is an endothermic process rather than exothermic so these reactions cannot be used as fuel for a star. Nucleosynthesis beyond Fe can occur in regions of intermediate (10^8 neutrons cm^{-2} s^{-1}) or high (10^{20} neutrons

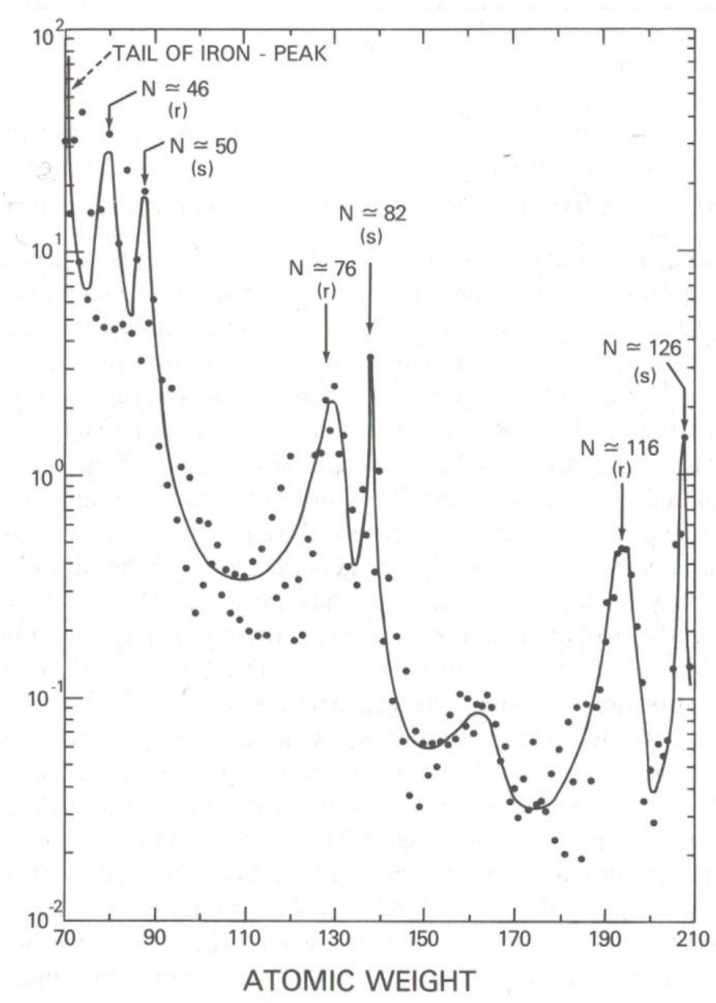

Figure 1.1: Cosmic abundances of the heavy elements as a function of atomic weight. [1, 2]

cm^{-2} s^{-1}) neutron flux. It was originally suggested by the abundance data of Suess and Urey [17] that nucleosynthesis reactions can occur by neutron capture up to $A = 238$. This was further supported by Cameron [1] in Figure 1.1 whose abundance data by atomic weight revealed sharp peaks at N = 50, 82 and 126 which correspond to the magic neutron numbers. The basic mechanisms for nucleosynthesis beyond Fe by neutron capture are the r- process and

the s-process. The basic mechanisms for nucleosynthesis beyond Fe by proton capture are the p and rp-processes.

1.1.4 Neutron Capture Processes

The coulomb barrier becomes very strong near the Fe peak resulting in charged particle cross sections to decrease dramatically around A $\cong$ 60 for moderate stellar temperatures. At the highest stellar temperatures charged particle reactions can occur but nucleosynthesis is more easily accomplished in this mass range by neutron capture processes since neutrons are not subject to the Coulomb force. There are two primary neutron capture models that describe well the abundances beyond the Fe peak, the *r(apid neutron capture)-process* and the *s(slow neutron capture)-process*. The primary difference between them is the rate at which neutron captures occur relative to the decay rate of the products.

A (n,γ) reaction results in a (Z, A) nucleus becoming a (Z, A+1) nucleus. If the product nucleus is unstable and the β decay constant is much greater than the time constant for successive (n,γ) reactions ($\lambda_\beta \gg \lambda_n$) then the product will decay to (Z+1,A). Under a slow neutron flux this chain will continue until the neutron capture cross section of the product nuclei becomes small such as at a neutron magic number. The neutron magic numbers represent "bottlenecks"in the s-process pathway through the chart of nuclides. Indeed the s-process model well reproduces the abundances of isotopes at N=50, 82 and 126 [3]. The s-process path will continue until ^{209}Bi which is the heaviest stable isotope. Further neutron captures are inhibited by α decays.

If we assume that neutron flux is very high such that ($\lambda_\beta \ll \lambda_n$) then the product nuclei may capture another neutron to go to (Z,A+2) before it can decay. Under this condition nucleosynthesis chains follow the r-process path which approaches the neutron dripline. The r-process is limited primarily by β decays near the neutron-drip line and by small neutron cross sections at the neutron magic numbers. Isotopes at the neutron magic numbers as the result of the r-process are more neutron rich than those produced by the s-process. Once the neutron flux decreases to allow β decays the r-process will "rain down" onto the valley of stability via β decay chains. The majority of neutron-rich stable isotopes are populated by these β decay chains.

Figure 1.2 depicts a section of the s-process pathway (solid line). In this section of the pathway we see that isotopes along the s-process are populated by both the s- and r- processes (via β decay chains) with the exception of ^{160}Dy which is "shielded" from the r-process by neighbouring nuclei because β decay chains cannot cross the valley of stability which lies along the s-process pathway. A nucleus produced only by the s-process is called an s-nucleus. Similarly those produced only by the r-process are r-nuclei. The r-nucleus ^{160}Gd is shielded from the s-process by neighbouring unstable nuclei which quickly β decay back to the valley of stability. Some stable nuclei are seen in the solar system abundance data which lie on the proton-rich side of the valley of stability. These nuclei are shielded from the s-process and cannot be produced by the r-process. These are p-process nuclei or p-nuclei originally thought to be the result of proton capture processes but are now likely explained by photodisintegrations.

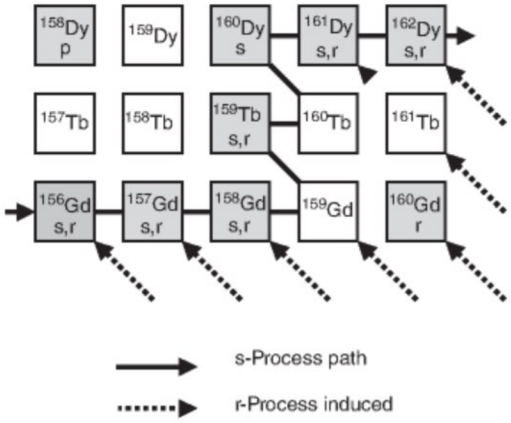

Figure 1.2: s-process path through Gd, Tb and Dy (solid line). Below the isotope symbol is an indication of which processes produce that isotope. Shaded squares represent stable isotopes while white squares are unstable. The dashed line represents r-process β decay chains "raining down" on the valley of stability once the neutron flux slows enough to allow β decays. Included is the p-nucleus ^{158}Dy which cannot be produced by either the r- or s- process. Figure adopted from [3].

1.1.5 Production of p-nuclei

Some neutron deficient nuclei above atomic mass 74 are shielded from neutron capture processes. These are *p(roton)-process* nuclei or *p-nuclei* originally thought to be the result of proton capture processes but are now likely explained by photodisintegrations, however some isotopes such as ^{113}In and textsuperscript115Sn are underproduced by this model. The abundances of p-nuclei are typically a factor of ~ 100 smaller than nearby abundances resulting from r- and s- processes and it is generally accepted that neutron capture process products are seeds for the p-process. Nearly all p-nuclei have even proton and neutron numbers, and those few without have very small abundances compared to other p-nuclei. There are three reactions allowing for neutron deficient nuclide production, the two most important being (p, γ) and

(γ, n). The third reaction is (p, n), however on the proton rich side of the valley of stability this reaction has a negative Q value and consequentially has a low reaction rate compared to the other two. For those isotopes resulting from (p, n) reactions r- and s- process seeds are not required. The p-process proceding via (p, γ) reactions would require very high temperatures and pressure $T \cong 2.5\ GK$ and $\rho \cong 100\ g/cm^3$ in an explosive environment such as that found in a supernova [18] but it is unlikely that these conditions could be found in the hydrogen rich zones of most stars [19]. These conditions as well as those required by the *r(apid)p(roton)-process* may be found in a type I X-ray burst [20] but it is unlikely that products could escape the powerful gravity of the neutron star surface so they do not to contribute to the cosmic abundances in Figure 1.1.

Instead of proton captures, it is now generally accepted that the p-process resulting in the observed cosmic abundances proceeds via photodisintegration (γ, n) reactions from r- and s- process seeds. These reactions require a *hot photon* environment such as those that exist in hydrogen exhausted stellar zones at temperatures of $T \cong 2 - 3\ GK$ [3]. Typically a p-process chain begins from a seed nucleus and proceeds to lower atomic masses via photodisintegration with reaction rates favouring even neutron numbers. This chain will typically proceed until further photodisintegrations become energetically unfavourable and the nucleus has an even neutron number. Sometimes the product nucleus is neutron deficient to the point where it becomes energetically favourable to proceed via the (γ, p) or (γ, α) reaction which often produces s- and r- process nuclei.

1.2 Thermonuclear Reactions

From the frame of reference of a particle, a thermonuclear reaction occurs with respect to the effective cross sectional area of the target particle. Consider a stellar plasma containing two particle types which are reacting. Since we are considering the astrophysical energy range ($\sim$ 150 - 1500 keV/u) we can neglect relativity in our description of these reactions. The reaction rate of the particles r_{12} is then:

$$r_{12} = N_1 N_2 \int_{v1} \int_{v2} (v_1 - v_2)\sigma(v_1 - v_2)\Phi_1 \Phi_2 d^3 v_1 d^3 v_2 \tag{1.1}$$

where N_1 and N_2 are the particles' respective number densities, v_1 and v_2 are their respective velocities and Φ_1 and Φ_2 are their Maxwell-Boltzmann velocity distributions:

$$\Phi_i = (\frac{m_i}{2\pi kT})^{3/2} exp(-\frac{m_i v_i^2}{2kT}) \tag{1.2}$$

In Equation (1.2) m_i is the particle mass, k is Boltzmann's Constant, and T is temperature. After a change of basis from (v_1, v_2) to (V, v) it can be shown that Equation (1.1) becomes dependent on the effective cross section $\sigma(v)$ [14]:

$$r_{12} = N_1 N_2 4\pi (\frac{\mu}{2\pi kT})^{3/2} \int_0^\infty v^3 \sigma(v) exp(-\frac{\mu}{2kT} v^2) dv \tag{1.3}$$

where μ is the reduced mass of the two-particle reaction. From the kinematics of a system of particles at energy E we can obtain the relationship between the center of mass energy and particle velocity:

$$E_{cm} = \mu v^2/2 \tag{1.4}$$

By substituting equation (1.4) into (1.3) we can find the thermonuclear reaction rate per particle pair:

$$< \sigma v >= \frac{r_{12}}{N_1 N_2} = \frac{8}{\pi\mu}^{1/2} (kT)^{-3/2} \int_0^\infty E_{cm}\sigma(E_{cm}) exp(\frac{E_{cm}}{kT}) dE \tag{1.5}$$

1.2.1 Non-Resonant Reactions

The fusion reaction rate of nuclei in a stellar environment is inhibited by the Coulomb barrier. Astrophysical energies are small and the Coulomb barrier becomes very strong at these low energies such that with a purely classical treatment of a collision, fusion reactions would be impossible. A quantum treatment allows for tunneling with a probability at astrophysical energies described by:

$$P_l(E) \propto exp(-2\pi \frac{2\pi Z_1 Z_2 e^2}{h} (\frac{\mu}{2E})^{1/2} \tag{1.6}$$

where h is Planck's constant. The reaction rate is increased with increasing tunneling probability. By adding together the contributions from the energy dependent Maxwell-Boltzmann velocity distribution which vanishes at high energies and the tunneling probability which is negligible at low energies we can define a narrow range of energies in which fusion reactions are likely to

occur. This range is the *Gamow window*. The Gamow window peaks at E_{eff} [2]:

$$E_{eff} = (2\pi^2 \frac{Z_1 Z_2 e^2 kT}{h} (\frac{\mu}{2})^{1/2})^{2/3} \tag{1.7}$$

and has an approximate width at half-maximum ΔE_{eff} of:

$$\Delta E_{eff} = (\frac{8 E_{eff} kT}{3})^{1/2} \tag{1.8}$$

Most non-resonant reactions occur with $E_{eff} \pm \Delta E_{eff}/2$. However reaction rates are typically dominated by resonant reaction rates which can only occur at specific energies within the Gamow window [14].

1.2.2 Resonant Reactions

So far in this brief discussion of thermonuclear reactions we have neglected the internal structure of nuclei. Nuclei have internal degrees of freedom in the form of the angular momenta of composite nucleons. Evidence of internal structure can be seen in the energy dependent cross section of thermonuclear fusion reactions where sharp peaks can be seen at specific energies. At these energies the probability of fusion is greatly enhanced and a reaction here is known as a *resonance capture* reaction. In a resonance capture reaction the product nuclei emerges in a transitional energy state. Typically it will emit at least one γ-ray as it relaxes to the ground state. The resonance reaction rate per particle pair can be described by [14]:

$$< \sigma v >= \hbar^2 (\frac{2\pi}{kT\mu})^{3/2} \omega exp(-\frac{E_r}{kT}) \tag{1.9}$$

where $\hbar$ is the reduced Planck's constant, E_r is the resonance energy, and $\omega\gamma$ is the *resonance strength.*:

$$\omega = \frac{2J_r + 1}{(2J_p + 1)(2J_t + 1)} \tag{1.10}$$

and,

$$\gamma = \frac{\Gamma_p \Gamma_\gamma}{\Gamma} \tag{1.11}$$

In Equations (1.10) and (1.11) the J values are the spins of the three nuclei and Γ is the sum of the partial widths of the entrance Γ_p and exit Γ_γ channels [14].

Because of the nature of the strong nuclear force and the many-body problem associated with nuclei it becomes incredibly difficult to predict the values of energy resonances. By measuring the resonance strengths of resonance capture reactions we can use Equation (1.9) to calculate the resonance energy of the reaction and ultimately describe the internal energy levels (and structure) of the nuclei. The resonance strengths are values which can be measured at TRIUMF's DRAGON laboratory which is the subject of Chapter 2. These resonance strengths can be calculated from laboratory yields. An accurate measurement of yields and accurate determination of resonance strengths therefore depends on the reliability and accuracy of the instrumentation at DRAGON.

In particular it depends on the ability of the end detectors to discriminate rare reaction products called *recoils* from a beam of particles.

1.3 Thesis Outline

DRAGON studies nuclear reactions involving radiative proton and alpha capture on proton-rich nuclei. The products of capture reactions will be measured using the hybrid detector which is the subject of this text. Chapter 2 discusses DRAGON and its instrumentation with a focus on the end detectors. Chapter 3 will discuss the interactions between radiation and matter for photons and charged particles. Chapter 4 will include the results of GEANT4 simulations as well as a description of the hybrid detector design. This detector will be described at the end of the following chapter.

Chapter 2

DRAGON

2.1 The DRAGON Apparatus

An apparatus for measuring resonance strengths of nuclear reactions in inverse kinematics to calculate reaction rates is located in the TRIUMF-ISAC radioactive ion beam facility. This chapter will outline this apparatus known as DRAGON (Detector of Recoils and Gammas of Nuclear Reactions) and discuss the limitations of its end detector. DRAGON is classified as a *recoil separator*.

Figure 2.1 is a schematic of the DRAGON apparatus. A succinct description of a typical DRAGON experiment is as follows. A beam of stable or radioactive nuclei in a single charge state is delivered by the ISAC linear accelerator to DRAGON. This beam reacts with H or He in the windowless gas target at a reaction-specific rate (often very low). A beam containing the reactant and product nuclei in a charge state distribution exits the windowless gas target and is filtered by charge-to-mass ratio by a sequence of electric and magnetic dipoles. After the gas target a magnetic dipole steers the beam

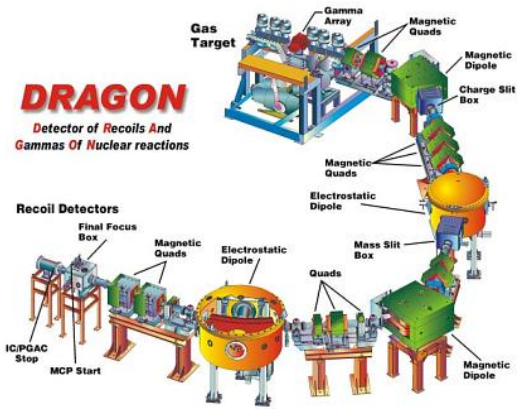

Figure 2.1: Detector of Recoils and Gammas of Nuclear Reactions (DRAGON).

through two slits to filter the beam by charge; then an electric dipole steers the beam through slits to filter by mass. This process is repeated through a second set of dipoles before terminating in an ion detector which (as of writing this report) is the experimenter's choice of an ionization chamber or a double-sided-silicon strip detector. Ideally only the product nuclei terminate in this detector; however that is never the case and it becomes the task of the end detector to discriminate recoils from the unreacted beam. If the delivered beam is radioactive it may contain isobaric contaminants which must also be discriminated from recoils.

2.1.1 Windowless Gas Target

The windowless gas target (see Figure 2.2) is a quadrangular aluminum cell with no physical barrier for ions entering and exiting the cell. Vacuum outside the cell is maintained by turbomolecular pumps. The target was designed to operate at 4 torr but can be run up to 8 torr. The upstream aperture has

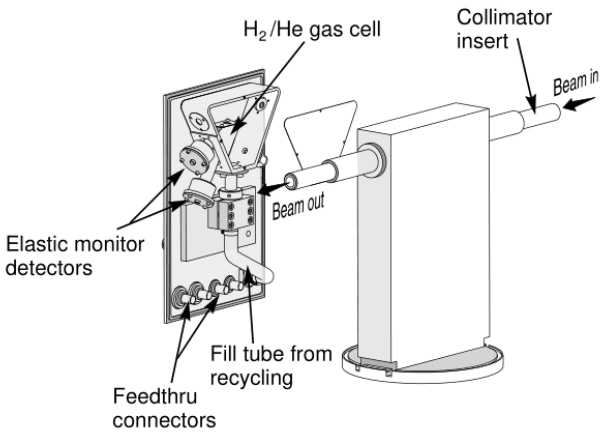

Figure 2.2: Schematic representation of the inner components of the DRAGON windowless gas target system. Figure adopted from [4].

a 6 mm diameter and the exit aperture has an 8 mm diameter. Although the distance between apertures is 11 cm, outflowing gas creates a non-uniform density profile resulting in an effective path length of 12.3 $\pm$ 0.5 cm [21]. The target gas is circulated through a Roots blower system (Leybold WSU2001, WSU501, WSU500) which sieves it through a zeolite gas trap and recirculates it. There are two hollow tubes terminating in Si barrier detectors (Ortec Ultra Cam, 150 mm^2 area) positioned at 30° and 57° from the beam line. These detect elastically scattered target particles for real time determination of beam intensity [4, 14].

2.1.2 BGO Detector Array

Surrounding the gas target is a hexagonally close packed array of 30 bismuth-germinate (BGO) scintillator detectors (see Figure 2.3a). These detectors are used to detect gamma rays in the range 1-10 MeV.

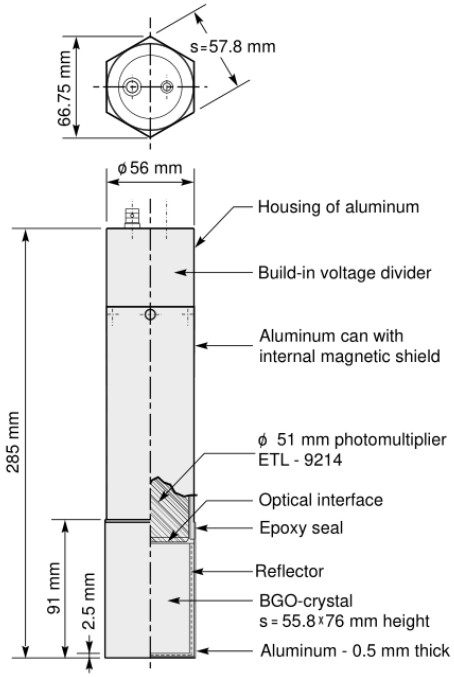

(a) One of the γ-ray scintillation detector composed of a BGO crystal coupled to a 51 mm diameter photomultiplier tube.

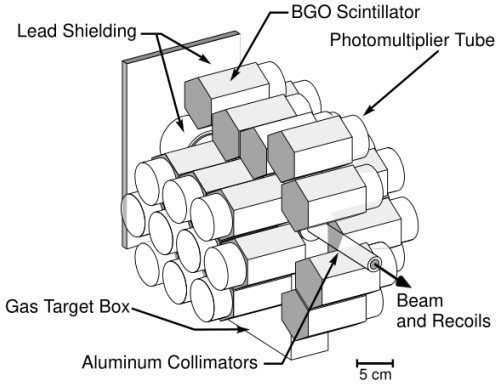

(b) The DRAGON BGO γ array, composed of 30 BGO units, surrounding the gas target region.

Figure 2.3: BGO Scintillators. Figures adopted from [4].

The array (see Figure 2.3b) covers 92% of the 4π solid angle about the center of the gas target with 60% of gammas depositing their entire energy in the BGO. Nuclear reactions often produce recoil nuclei in an excited state. When they relax they can produce gamma rays which are measured by this array. Measurements of coincidence events between the BGO array and the end detector are used to filter non-recoil events during data acquisition [4, 14].

2.1.3 Electromagnetic Separation

Ions exiting the gas target are confined to a recoil cone and are a charge distribution. Energy straggling through the gas target also produces an energy distribution in the beam. The recoil separator is a sequence of electric and magnetic dipoles separated by quadrupoles and sextupoles that steer recoils away from the beam into the end detector. Following the gas target are two quadrupoles which focus the beam cone into the first magnetic dipole. Once entering the magnetic field the Lorentz force steers them into circular paths of radius R described by:

$$R = \frac{mv^2}{qvB} \tag{2.1}$$

where R is proportional to the ion's mass m, velocity v and charge q. Positioned beyond MD1 are movable slits called charge slits. Since ions differ by their momentum-to-mass ratio recoils can be steered through these slits. Beyond these slits the beam, including recoils, ideally consists of a single charge-state. The beam is refocused by three quadrupoles and two sextupoles into an electrostatic dipole. The beam is steered between two arcing plates at high voltage (100 kV). The ions are accelerated in the direction of the center of the radius of curvature of the arced plates according to their charge to mass ratio. They follow a circular path of radius R according to:

$$R = \frac{mv^2}{q\epsilon} = \frac{2E}{\epsilon} \tag{2.2}$$

where ϵ is the electric field strength and E is the ion kinetic energy. As with MD1 just beyond ED1 are two slits called mass slits. Ions with a desired kinetic energy are selected by steering them through the mass slits. These two stages of separation are repeated in the second half of the recoil separator and a final set of two quadrupoles focuses the beam into the end detector which can be currently be an ionization chamber or a double-sided-silicon-strip detector. This thesis will propose a new hybrid detector which combines the strengths of both of these detectors . These strengths will be discussed in the later sections.

2.1.4 Local Time-of-Flight Measurement

At the focal point of the recoil separator a Micro-Channel-Plate (MCP) detection system has been implemented to measure the local time-of-flight of beam and recoil particles entering the end detector. A time-of-flight measurement of incoming particles can help suppress the leaky beam by providing an additional method of separating recoil particles from the beam. This is done by analyzing the Et^2 spectrum of the incoming particles where t is the time difference between signals produced in two fast timing systems positioned on the beamline and E is measured by the end detector. MCPs were chosen as the fast timing detectors due to their excellent timing capabilities [5].

The signal produced by the fast timing system originates from electrons knocked off the two thin carbon foils (20 μg/cm^2) perpendicular to the beam line located between the last set of quadrupoles and the end detector. Ions deposit energy in the foils releasing electrons which are accelerated to a system

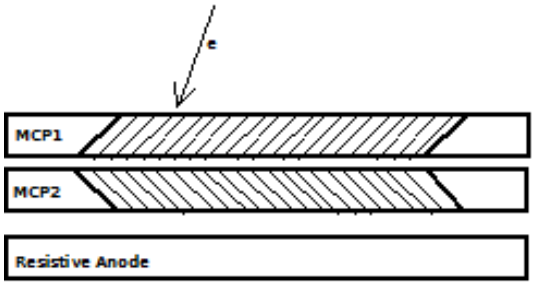

Figure 2.4: Schematic of the electron amplification system of the fast timing system. Each system consists of two MCPs in the chevron configuration with capillaries at an angle of 8°from the normal to the plane of the MPC. Incoming electrons are amplified by the two MCPs and collected by the RAE. Adapted from [5].

of four grids which act as an electrostatic mirror which deflect the electrons towards two MCPs (see Figure 2.4). An MCP consists of an array of small diameter (10 μm) glass capillaries through which incoming electrons are accelerated by a $\sim$ 1 kV bias. The inside surface of these capillaries are coated with a material that produces secondary electrons when an electron collides with it. This means that each capillary acts like a small electron multiplier tube amplifying the signal produced by the carbon foils.

Each MCP at DRAGON is a 3394A MCP/RAE (resistance anode encoder) sensor purchased from Quantar Technology Inc in 1999 [22]. Each of the two fast timing systems consists of a carbon foil, an electrostatic mirror and two MCPs in the chevron configuration in which two MCPs are placed on top of each other and their glass capillaries are oriented away from each other at 8° from the MCP normal. This configuration was chosen to limit the loss of resolution from the ionization of residual gas in the capillaries and in the junction between MCPs.

2.2 General Properties of Radiation Detectors

The DRAGON facility includes scintillation, ionization and silicon diode detectors. Before describing these I will first introduce concepts relevant to all types of radiation detectors. These will include three operating modes and the situations in which they are most useful as well as the concept of energy resolution.

All radiation detectors operate in a similar way. A single particle of radiation such as an ion or γ-ray interacts with matter in the sensitive region of the detector to generate electric charges. These charges are then accelerated through an electric field to produce a charge-dependent signal. There are three common modes of operation shared by all radiation detectors, which are current mode, mean squared voltage (sometimes called Campbell [23]) mode, and pulse mode [6].

2.2.1 Current Mode

If we assume that the response time of the detector T remains constant then the signal current will be the time average $I(t)$ of individual current pules $i(t)$.

$$I(t) = \frac{1}{T}\int_{t-T}^{t} i(t^{'})dt^{'} \tag{2.3}$$

From Equation (2.3), operating with a large response time will minimize variance in the signal. The drawback to large response times is insensitivity to

rapid changes in event rate and current amplitude. Even with a mono-energetic source, fluctuations in charge-pair production occur because of statistical fluctuation in radiation energy loss. Charge generation behaves as a Poisson distribution. For the case of a mono-energetic source the standard deviation σ of n events that are occuring at a rate r with an effective measurement time T is:

$$\sigma_n = \sqrt{n} = \sqrt{rT} \tag{2.4}$$

The average current I_0 is given by:

$$I_0 = rQ = \frac{rEq}{w} \tag{2.5}$$

where $Q = Eq/w$ is the charge produced in each event, E is the average energy deposited per event, w is the average energy required to produce a unit charge pair, and q is the fundamental charge. A detector used for measuring background radiation levels such as a Geiger counter operates in pulse mode because the time between events is longer than the detector response time. If an ionization chamber is being used to measure high event rates it should be operated in current mode because of the long (ms) response time of an ionization chamber. Figure 2.5 depicts a simple current mode signal from a mono-energetic source. The time average of the fluctuations around I_0 is the standard deviation of the signal. This fluctuation is the result of σ_n, random noise in the detector and instrument drift [6].

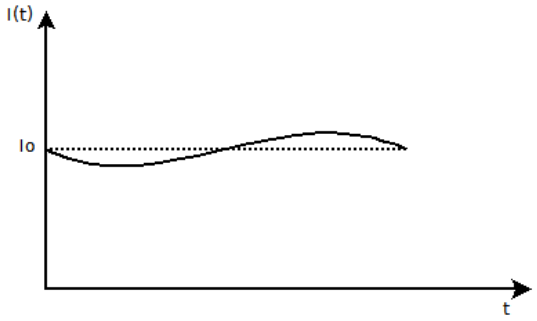

Figure 2.5: Current mode signal from a monoenergetic source with a high event rate. The average current I_0 is the product of the event rate and the charge produced per event. The real signal I(t) fluctuates around this due to the statistical nature of charge generation and detector response (adapted from [6]).

2.2.2 Mean Square Voltage

An analysis of mean square voltage (MSV) operation was first given by Campbell and Francis in 1946 [23]. If we start with a current like the one in Figure 2.5 then add circuit components to block I_0, MSV operation analyzes the σ_I of the current. The fractional standard deviation in the signal is given by:

$$\frac{\sigma_I(t)}{I_0} = \frac{\sigma_n}{n} = \frac{1}{\sqrt{rT}} \tag{2.6}$$

If we combine Equations (2.5) and (2.6) we predict the MSV signal to be proportional to the square of the charge generation:

$$\sigma_n^2(t) = \frac{rQ^2}{T} \tag{2.7}$$

In this case we assume Q to be constant so MSV should be used in cases where fluctuations in Q are small compared to those in arrival time. The power of

MSV mode is best realized in mixed radiation environments. Since the signal is proportional to the square of the charge produced, radiation types can be discriminated from each other. The detector response will be much greater for a radiation type producing even a small amount of additional charge over another type. MSV detectors are often seen in Nuclear Reactors where multiple forms of radiation such as alphas, neutrons and gammas are expected [6].

2.2.3 Pulse Mode

Pulse Mode operation is typically used for low event rate measurements such that the time between events is greater than the detector response time. The shape of the pulse is dependent on the time constant $\tau = RC$ of the circuit where R is the input resistance of the preamplifier connected to the detector and C is the total capacitance of the detector, all circuit components up to the preamplifier, and the preamplifier itself. The pulse height V_{max} is directly proportional to the charge generated by a single event.

$$V_{max} = \frac{Q}{C} \tag{2.8}$$

τ is typically chosen to be much greater than the collection time of the detector so that very little current flows in the load resistance. Provided the time difference between pulses is large the capacitor discharges through the resistance, and the voltage across R goes to zero. The relatively slow discharge of a detector operating in this mode contains accurate energy information. By choosing τ to be less than the collection time of the detector this can be

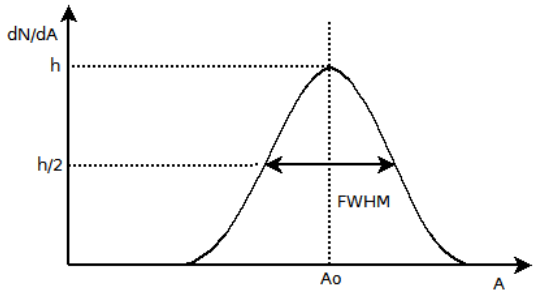

Figure 2.6: Example of a differential pulse height spectrum. The spectrum in this case was a Gaussian distribution with standard deviation σ. The FWHM is 2.35σ

sacrificed in favor of timing information for measurements of high event rates. From Equation (2.8) we see that variation in the pulse height must correspond to a variation in either detector response or radiation energy [6].

2.2.4 Energy Resolution

Information on the variation in pulse height is contained in the *differential pulse height distribution*. The differential pulse height distribution is the differential number dN of pulses observed with a differential amplitude dA plotted against the amplitude A. The differential pulse height spectrum from a mono-energetic energy source is the *response function* of the detector. The number of pulses between two amplitudes A_1 and A_2 can be found by integrating under the curve of the differential pulse height distribution. Figure 2.6 depicts an example of a response function with Gaussian form.

Multiple pulses measured by a pulse mode detector can overlap. The ability of the detector to discriminate between the two pulses is described by its

resolution R obtainable from the response function. The formal definition of the energy resolution is:

$$R = \frac{FWHM}{A_0} \tag{2.9}$$

A narrow peak in the response function corresponds to a well-performing detector with high resolution and a wide peak corresponds to poor resolution. The FWHM of the peak arises from the fluctuations of pulses generated by events depositing the same energy in the detector. Fluctuations in the response of a detector can arise from the drift of operating characteristics of the detector, random noise and statistical noise from the Poisson nature of charge generation. The statistical nature of charge generation is likely to be the smallest contribution to the FWHM of the response function. By considering the Poisson nature of the events we can determine the statistical limit of the resolution. Assuming a Poisson distribution, the standard deviation of the formation of N charge carriers is $\sqrt{N}$. Most detectors have a linear response function so pulse amplitudes are proportional to some constant D and N. Considering this we can determine the Poisson limit of the detector:

$$R_{poisson\ limit} = \frac{FWHM}{H_0} = \frac{2.35D\sqrt{N}}{DN} = \frac{2.35}{\sqrt{N}} \tag{2.10}$$

This assumes processes that give rise to the formation of individual charges are independent. Precise measurements of the statistical limit of R reveal deviations of up to a factor of four which suggests that these processes are not

independent. The deviation from the expected Poisson distribution behavior is described by the *Fano factor* F:

$$F = \frac{observed\ variance\ in\ n}{Poisson\ predicted\ variance} \tag{2.11}$$

We can then redefine Equation (2.10) to take take into account the Fano factor.

$$R_{statistical\ limit} = 2.35\sqrt{\frac{F}{N}} \tag{2.12}$$

F is typically very small for semiconductor detectors but can approach unity for scintillation detectors. This means that scintillation detector response is nearly consistent with the response expected from the Poisson statististial treatment of charge-pair production [6].

2.3 End Detectors at DRAGON

2.3.1 Ionization Chamber

Three of the commonly used gas detectors are the ionization chamber, proportional counter and Geiger counter. A gas detector is an ionization chamber if the chamber is not operated at a voltage high enough for the signal to be amplified by electron cascades. The DRAGON ionization chamber consists of 25 anode strips which are soldered together in a 10 cm, a 10 cm and a 5 cm configuration to form 3 sensitive regions in the ionization chamber.

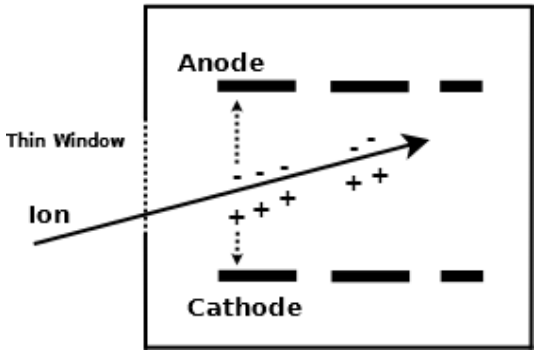

Figure 2.7: Schematic of an ionization chamber. Included is the path of an ion through a volume filled with gas and the production of electron-ion pairs. An electric field is generated by parallel plates held at a constant potential.

The segmentation allows for isobaric separation and identification according to stopping power which will be further discussed in Chapter 3. Isobaric separation is possible in an ionization chamber even if the isobars have nearly equal energy. This is the advantage of an ionization chamber over a semiconductor detector at the cost of resolution.

Figure 2.7 depicts a schematic of an ionization chamber. When an ion passes through a gas it liberates electrons from the surrounding medium generating electron-ion pairs. Pair generation is the primary interaction an ion will have with its gas medium. The signal produced by charge drift is the source of information derived from an ionization chamber because there is a direct correlation between the number of ion pairs formed and the energy deposited by the ion. The energy required to create an ion pair is not simply the ionization energy of the gas because secondary processes (which will be discussed in Chapter 3) can occur so a value of interest when choosing a gas is the average energy dissipated per ion pair (w value) of the gas.

When an ion passes through a gaseous medium a *charge cloud* is formed. This cloud will slowly diffuse away from the ion path. *Charge transfer collisions* can occur when a neutral particle collides with a positive ion. An electron transfer can occur such that the species swap charges. In a mono-species gas these interactions are less relevant; however in gas mixtures charge transfers tend to ionize the species with the lowest ionization energy. If a free electron or negative ion collides with a positively charged ion a neutral particle can result: this is called *Recombination*. Neutral particles do not contribute to the output signal so recombination can reduce signal strength. The recombination rate is proportional to the product of the species concentrations.

$$\frac{dn^+}{dt} = \frac{dn^-}{dt} = -\alpha n^+ n^- \tag{2.13}$$

Here α is the recombination coefficient. α is orders of magnitude larger for positive-negative ion collisions than it is for electron-ion collisions. Most recombination occurs soon after pair generation around the ion track when charge density is the highest. This is called *columnar recombination*. Recombination outside the column where the pairs were generated is *volume recombination*. In the case of multiple particle tracks, charges can drift through other electron clouds, and this is the dominant source of volume recombination effects. The magnitude of this effect will increase for high irradiation rates.

Recombination will eventually neutralize all charge carriers in the volume but columnar recombination can be mitigated by applying an electric field. This will cause positive and negative charges to drift away from each other with a drift velocity described by:

$$\mathbf{v} = \mu \frac{\mathbf{E}}{p} \tag{2.14}$$

where p is the gas pressure and μ is the particle mobility. With high $\|\mathbf{E}\|$ columnar recombination can be made negligible. Moving charges induce a current in the anode circuit. It is this *ionization current* which is the source of the signal read off the anode. The ionization current increases in magnitude with $\|\mathbf{E}\|$ as columnar recombination decreases. As $\|\mathbf{E}\|$ increases, *saturation* is reached when charges are depleted in a gas and the ionization current can increase no further. If $\|\mathbf{E}\|$ continues to increase, high velocity electrons can cascade which greatly amplifies signal strength proportional to the number of ion pairs. In this field region the chamber is operating as a proportional counter. At even higher operating potentials cascades proceed until enough positive charges are produced to counter the electric field. This means that all pulses will be of the same height and it becomes impossible to know the incoming ion energy.

Because electrons have a low mass their mobility is around 1000 times higher than an ion. This means that the typical collection time for electrons is on the order of microseconds and ions are on the order of milliseconds. When reading the output of an ionization chamber, the experimenter can take the signal induced by the electrons or by the positive ions. Electrons will have a very short collection time and ions will have a high collection time.

Because ion track positions are dependent on the incoming beam, for anything but a pencil beam these positions will vary. This will create a fluctuation in ionization current for different tracks of the same ion species and energy.

In pulse mode this will serve to generate multiple pulse heights for the same species. In the case of the DRAGON ionization chamber and the hybrid ionization chamber this problem is solved by the inclusion of a Frisch Grid. A Frisch grid divides the chamber volume into two regions. The Frisch grid consists of a conducting grid held at a constant voltage between that of the anode and the cathode. Because of the position of the window all charge pairs are generated in the region between the Frisch grid and the cathode. The grid is made to be transparent to electrons. The location of the load resistor in the ionization current circuit is chosen such that the signal is not induced by charges between the Frisch grid and cathode but only between the grid and the anode. In this way the signal is induced by electrons all accelerated through the same distance in the gas volume.

In the case of a parallel plate geometry, the capacitance of the detector is:

$$C = \frac{\epsilon A}{d} \tag{2.15}$$

where A is the plate area and d is the distance between the plate and the cathode or the Frisch grid. The signal induced in the anode by a single event is then:

$$V_{\max} = \frac{n_0 e}{C} \tag{2.16}$$

where n_0 is the number of original ion pairs and e is the electron charge [6].

2.3.2 Double-Sided-Silicon-Strip Detector (DSSSD)

The usefulness of an ionization chamber is limited by its relatively low resolution. If we recall Equation (2.10) we see that resolution is inversely proportional to the square root of N. This means that the resolution is directly proportional to the average energy per charge pair (w value) of the detector. In semiconductor diode detectors the charge pairs are electron-hole pairs and the number of these pairs generated by an ion track are orders of magnitude greater than that same track in a gas medium. This can in part be attributed to the fact that solids are around 1000 times greater in density than gases. Other features of a semiconductor detector are its small size, fast collection time and its thickness which can be easily selected according to its application. Unlike a gas detector the sensitive material in a solid state detector cannot be changed or recycled so this type of detector is subject to performance degradation over time as well as radiation damage if beam intensities are too great [6].

The DRAGON ionization chamber uses isobutane gas which has a w value of 23 eV [24, 25]. This value in Si is 3.62 eV [26]. According to Equation (2.10) this means we expect a semiconductor detector to have superior resolution by a factor of 2.5 in the Poisson limit. This factor is expected to be larger if the Fano factor is considered because solid detectors typically have a smaller Fano factor than gaseous detectors.

The DSSSD used at DRAGON and in the hybrid detector is the double-sided-silicon-strip detector Micron Semiconductor Model W(DS)-250 (see Figure 2.8). It consists of two layers of 16 Si strips oriented perpendicular to each other. These strips have 3.1 mm pitch and 5 cm length with a gap of

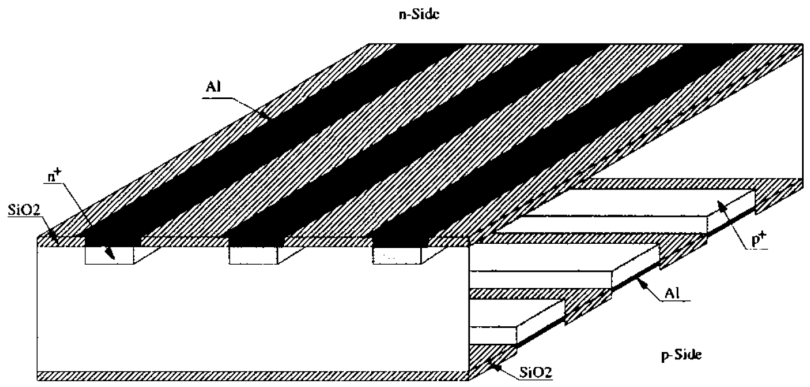

Figure 2.8: Exploded schematic view of a DSSSD. The detection strips are oriented orthogonal to each other. Also pictured is the insensitive "dead-layer" of Al covering the sensitive Si. Dimensions are not to scale. Figure adopted from [7].

approximately 110 μm between them. This gap is filled with insulating material. The strips are 300 μm thick which is much larger than the typical range of a heavy ion which is on the order of 10s of μm. The rear strips are then far from the site of charge creation resulting in relatively poor energy resolution and timing compared to the front strips. Because the EM separator's steering instruments bend the beam horizontally the front strips are oriented vertically to measure horizontal position information [4, 27].

In a gas detector, electron mobility is much greater than ion mobility but in a semiconductor detector electrons and holes have almost the same mobility. Operated at saturation the drift velocity of these charge carriers is on the order of 10^7 cm/s so for a maximum distance of 300 μm that is a collection time of 3 ns, six orders of magnitude less than the collection time of an ionization chamber. The silicon detector is capable of running at very high event rates with high energy resolution. However if two ions have the same mass and

nearly the same energy as is often the case in a recoil separator it may not be able to discriminate between the two. A semiconductor detector usually stops heavy ions so it only measures total energy. An ionization chamber can measure energy loss which is A, Z and energy dependent so it is capable of discriminating between isobars. This will be further discussed in Chapter 3.

2.3.3 The Strengths of a Hybrid Detector

The Hybrid detector described here will act as a superior ΔE-E detector to either the ionization chamber or DSSSD operating alone. As discussed in the previous sections, ionization chambers and DSSSDs have their own strengths and weaknesses. An ionization chamber has relatively poor resolution compared to the DSSSD but compensates for this with the ability to discriminate recoils from isobaric contaminants by their energy loss signal. A DSSSD has superior energy resolution, timing capabilities, and produces a strong E signal but is often unable to separate isobars which are very close together in kinetic energy. The Hybrid detector will consist of an ionization chamber set in front of a DSSSD along the beam axis to act as a superior ΔE-E end detector that can discriminate isobaric contaminants from the beam particles and from the recoils while preserving high resolution and fast timing capabilities.

Chapter 3

The Interactions of Radiation With Matter

All radiation detectors operate by producing a current in response to the interaction of some particle of radiation with the sensitive material of the detector which produces charge-pairs. DRAGON has scintillator detectors for detecting photons, and an ionization chamber and semiconductor detector for detecting ions. In this chapter I will describe the ways these radiation types can interact with matter and how these interactions produce charges in the sensitive material of the detector.

3.1 Photon Interactions with Matter

There are three interactions of photons in matter that are important for radiation detectors. These are *photoelectric absorption*, *Compton scattering*, and *pair production*. Each of these interactions result in the transfer of the photon's energy into energetic charged particles. Unlike massive neutral particles which are usually slowed by their interactions (with relatively rare scattering

events), photon interaction always involves the destruction or scattering of the photon. As a result an important distinction between the passage of photons and the passage of charged particles is that a beam of photons attenuates only in intensity and not in energy during passage. Inelastic collisions with charged particles while maintaining direction is not possible due to a photon's lack of charge.

3.1.1 Photoelectric Absorption

Photoelectric absorption or the *photoelectric effect* is the ejection of an electron from an atom after absorption of a photon. The energy of this electron is described by:

$$E_{\mathrm{e^-}} = h\nu - E_{\mathrm{b}} \tag{3.1}$$

where h is Planck's constant, ν is the photon frequency and E_b is the binding energy of the electron. This effect will always occur in an atom or ion because a free electron cannot absorb a photon.

As seen in Figure 3.1, above the highest binding energies of an atom the cross section for the photoelectric effect drops off significantly. The highest energy peak in cross section is known as the K-edge. Electrons ejected at this energy are K-shell electrons. Provided photons have sufficient energy K-shell ejections are the most common result of photoelectric absorption. In non-relativistic cases the cross section for photoelectric absorption very close to the K-edge (ν_k) can be described using a Born approximation [8]:

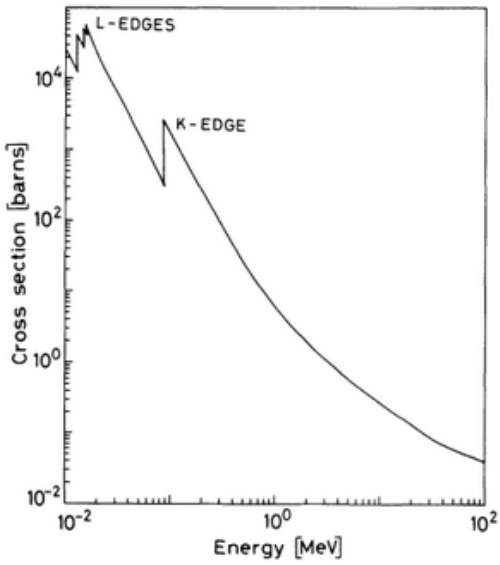

Figure 3.1: Calculated photoelectric cross section for lead [8].

$$\phi_{photo} = \frac{6.3 \times 10^{-18}}{Z^2}(\frac{\nu_k}{\nu})^{8/3}[barns] \tag{3.2}$$

After an electron leaves the atom an x-ray is emitted either through free electron capture or re-arrangement of electron shells. In a small fraction of cases the X-ray can be substituted by an Auger electron. A rough approximation of the probability of photoelectric absorption τ over all photon energies $h\nu$ is given by [6]:

$$\tau \cong const(\frac{Z^n}{E_\gamma^{3.5}}) \tag{3.3}$$

where n ranges between 4 and 5. The Z dependence of τ is the reason why high Z materials are desirable in gamma-ray shielding.

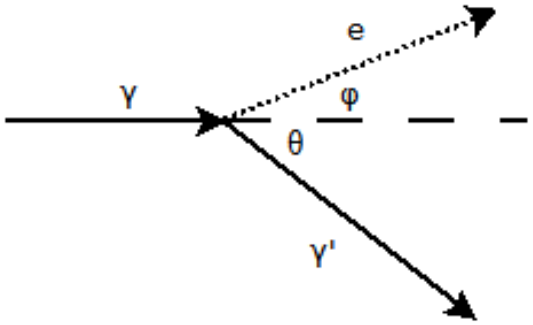

Figure 3.2: The inelastic collision between an incident photon and an electron at rest. This is the Compton scattering interaction.

3.1.2 Compton Scattering

The Compton scattering interaction takes place between an incident photon and an electron. In the rest frame of the electron, (termed the *recoil electron*) the gamma ray transfers energy to the electron. The photon is scattered at an angle θ and the recoil electron is scattered at the angle ϕ (see Figure 3.6).

The final energy of the scattered photon is:

$$h\nu^{'} = \frac{h\nu}{1 + \frac{h\nu}{m_0c^2}(1 - cos\theta)} \tag{3.4}$$

where m_0c^2 is the rest-mass energy of an electron. The electron can usually be treated as if it were at rest if the photon energy is much greater than m_0c^2. The photon is never destroyed in this interaction even in the event of $\theta = 180°$. A high energy electron can ionize material during passage creating charge pairs. The cross section for Compton scattering is known as the *Klein-Nishina* formula and it was one of the first cross sections calculated using quantum electrodynamics [8, 28]:

$$\frac{d\sigma}{d\Omega} = \frac{r_e^2}{2}\frac{1}{1+\kappa(1-cos\theta)^2}(1+cos^2\theta+\frac{\kappa^2(1-cos\theta)^2}{1+\kappa(1-cos\theta)}) \tag{3.5}$$

where r_e is the classical electron radius, and $\kappa = (h\nu)/(m_0c^2)$. The maximum electron recoil energy allowed by this interaction (and maximum energy that can be deposited in the medium as charge pairs) is known as the *Compton edge* [8]:

$$T_{max} = h\nu\frac{2\kappa}{1+2\kappa} \tag{3.6}$$

Since this interaction depends on electron-photon interactions, high Z materials are necessary for compton scattering detectors [6].

3.1.3 Pair Production

Pair production is the conversion of the energy of a photon into an electron-positron pair in the presence of a nucleus (see Figure 3.3). For pair production to be possible the incoming gamma ray must have a minimum energy of twice the electron rest mass (1.02 MeV). Pair production becomes more dominant at higher energies. Pair production always destroys the incoming photon so excess energy above 1.02 MeV is transformed into the kinetic energy of the charge pairs. The positron produced soon annihilates with another electron producing two annihilation photons. This means that the net result of pair production is two charge-less photons and an ionizing electron.

Photon detectors in nuclear physics experiments are usually some type of scintillator. An absorbing material is a scintillator if it produces visible light

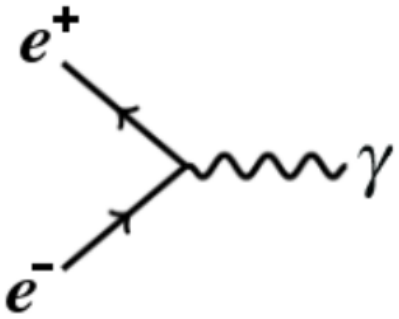

Figure 3.3: Feynman diagram of pair production.

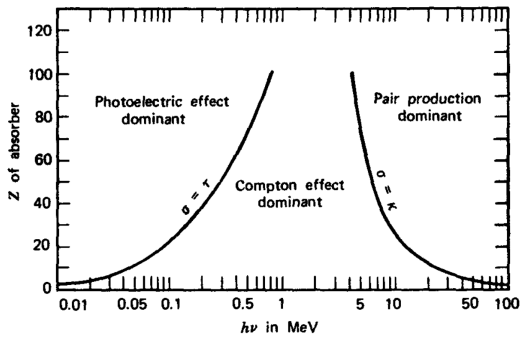

Figure 3.4: Energy regimes describing the relative importance of the three major photon interactions described in this chapter. The lines correspond to Z and $h\nu$ values where neighboring interaction have equal probability. [9]

from incoming radiation, usually γ-rays. A γ-ray typically enters the scintillating material and produces electrons through one or more of the three interactions described in this chapter. These electrons excite the absorbing material during passage which quickly relaxes giving off visible light. This light is absorbed by a photocathode on the other side of the scintillating material and produces electrons. Each electron enters a photomultiplier tube and reflects off a series of dynodes coated with a material which produces secondary electrons. Photomultiplier tubes can produce 10^6 electrons for every electron released by the photocathode.

The relative importance of each interaction in the production of ionizing radiation depends on the energy of the incoming gamma-ray as seen in Figure 3.4. As mentioned at the beginning of this chapter, a beam of photons passing through an absorbing material attenuates only in intensity and not energy because photon interactions result in either the scattering or destruction of the photon. The intensity I of an attenuating beam with initial intensity I_0 is an exponential [6]:

$$\frac{I}{I_0} = e^{-\mu t} \tag{3.7}$$

Here μ is the *linear attenuation coefficient* and is the sum of the individual energy dependent attenuation coefficients for the photoelectric effect, Compton scattering, and pair production. The *mean free path* λ of a photon is the average distance traveled by a photon before it interacts with an absorber [6]:

$$\lambda = \frac{\int_0^\infty x e^{-\mu x}}{\int_0^\infty e^{-\mu x} dx} = \frac{1}{\mu} \tag{3.8}$$

3.2 Charged Particles

Unlike uncharged particles like photons and neutrons, charged particles are all subject to the Coulomb force. In this section I will be discussing ions which are heavy charged particles and electrons. Recall that a beam of photons passing through a medium will attenuate only in intensity and not in energy. A beam of ions passing through a medium will attenuate in energy and only in some cases attenuate in intensity. If we consider the case of a heavy ion beam

passing through a thin gas target, in the absence of nuclear reactions the ions are too heavy to be deflected significantly by relatively light gas particles but the ions will interact with many electrons in the target through the coulomb force. If an atom is near the passing ion, its electron shell configuration can shift into a higher energy state (*excitation*) or an electron can be removed from the atom (*ionization*). These events occur at the expense of the kinetic energy of the ion acting as a sort of electromagnetic drag force. The maximum energy that can be transferred to an electron in an ion-electron collision is about 1/500 [6] of the kinetic energy per nucleon of the ion. This means that many excitations and ionization events will occur creating charge-pairs in the medium in the case of ionization events. The energy deposited in the medium is then the average energy per ion pair (w-value) of the ion in the gas multiplied by the number of charge pairs produced. This is the mechanism ionization chambers and semiconductor detectors use to measure heavy ion energy. Because these electron-ion interactions occur over long distances in all directions simultaneously in the material they do not appreciably deflect a passing ion unless the ion has low energy and is stopping in the gas. The distance a charged particle can travel in a medium is that particle's *range*.

The total energy loss of an ion passing through a medium is the sum of radiative and collisional energy losses. Radiative energy losses are typically small for ion passage but become relavent for light particles like electrons and positrons. Collisional losses include inelastic collisions with atomic electrons and elastic collisions with absorber nuclei. Radiation losses include Cherenkov radiation, and Bremsstrahlung radiation. Contributions from inelastic col-

lisions and Cherenkov radiation are included in the description of an ion's stopping power.

3.2.1 Stopping Power

The *linear stopping power* (also called *specific energy loss*) S is the rate of energy loss of an ion passing through an absorber. S is described by the *Bethe-Bloch formula* [8].

$$S = -\frac{dE}{dx} = 2\pi N_a r_e^2 m_e c^2 \rho \frac{Z}{A}\frac{z^2}{\beta^2}[ln(\frac{W_{max}}{I^2} - 2\beta^2 - \delta - 2\frac{C}{Z}] \qquad (3.9)$$

where

r_e: classical electron radius = 2.817×10^{-13} cm

ρ: density of absorbing material

m_e: electron mass

z: charge of incident particle in units of e

N_a: Avogadro's Number 6.02×10^{-23}

β: v/c of the incident particle

I: mean excitation potential

δ: density correction

Z: atomic number of absorbing material

C: shell correction

A: atomic weight of absorbing material

$W_{max} \simeq 2m_e c^2(\beta\gamma)^2$: maximum energy transfer in a single collision

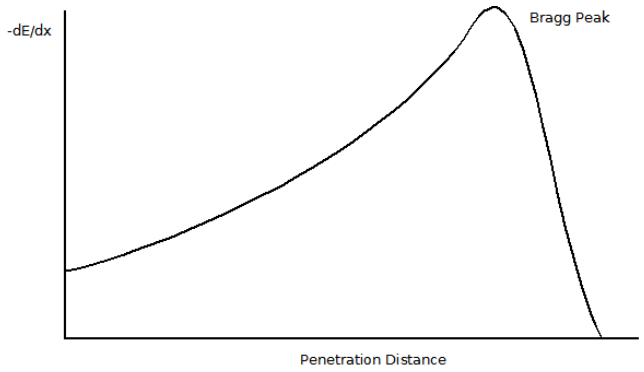

Figure 3.5: Typical specific energy loss behavior along an ion track. The Bethe-Bloch formula only applies to the approximately linear region.

$\gamma = \frac{1}{1-\beta^2}$: Lorentz factor

δ and C are correction factors for high and low energies respectively. In Figure 3.5 we see that the specific energy loss changes with depth with a peak near the end of the particle track. As the ion slows, charges from the absorbing medium accumulate around it. The shape of this *Bragg peak* seen in Figure 3.5 roughly corresponds to what one expects from the Z^2 dependence of S. In the case of a beam of ions the Bragg peak is less pronounced, which is due to *energy straggling*. Energy loss is a stochastic process so a beam of ions results in a spread of energies deposited in the medium. The width of this distribution is its energy straggling. Energy straggling and low energy deflections contribute to *range straggling* which widens the Bragg peak. For the case of a thin absorber (such as a mylar window) the energy deposited in the absorber is:

$$\Delta E = (-\frac{dE}{dx}_{avg})t \tag{3.10}$$

where t is the absorber thickness. $(-dE/dx)_{avg}$ is the specific energy loss avereaged over the width of the absorber. In the case of a mylar window this energy loss is small and the stopping power can be calculated from the incident energy.

We also see in Equation (3.9) that the specific energy loss is dependent on A, Z, and v which are related to kinetic energy. In particular the A dependence allows a gas detector to differentiate between isobars with nearly equivalent specific energy provided the ion track does not enter the Bragg peak region. This discrimination power is the upside to using an ionization chamber for ion detection at the cost of energy resolution.

3.2.2 Radiative Losses

Cherenkov radiation appears when a charged particle in an absorber travels faster than the speed of light in that absorber. This speed is described by:

$$\beta c = v = \frac{c}{n} \tag{3.11}$$

where n is the index of refraction. The condition for Cherenkov radiation is then $v > c/n$. An electromagnetic shockwave analogous to a sonic boom is generated by the passing ion, and this shockwave is Cherenkov radiation. Its contribution to the specific energy loss is greatest at relativistic energies but still small (on the order of 10^{-3} MeV cm^2 g^{-1} [8]). Usually it is negligible compared to energy loss from electromagnetic collisions.

Bremmsstrahlung Radiation or *braking radiation* is produced whenever a charged particle is deflected by another charged particle or external electric or magnetic field. The emission probability is inversely proportional to the square of the particle mass. This means that Bremsstrahlung radiation contributes substantially only for light particles like electrons and positrons. The energy contribution by Bremsstrahlung radiation is:

$$-(\frac{dE}{dx})_{rad} = NE_0\Phi_{rad} \tag{3.12}$$

where N is the number of atoms/cm^3. For the case in which the electron initial energy E_0 is greater than the electron mass energy but less than $137m_ec^2Z^{1/3}$:

$$\Phi_{rad} = 4Z^2r_e^2\alpha(ln\frac{2E_0}{m_ec^2} - \frac{1}{3} - f(Z)) \tag{3.13}$$

Here *f(Z)* corrects for the Coulomb interaction of the emitting electron in the electric field of the nucleus [8].

Chapter 4

Detector Development and GEANT4 Simulation Results

4.1 GEANT4

Physical parameters of the hybrid detector were determined using GEANT4. GEANT4 is a Monte-Carlo simulation toolkit developed at CERN used to simulate high energy particle detectors [29]. GEANT4 physics is handled by physics lists. When writing a new application the developers can either implement their own physics list or use physics lists included in the GEANT4 installation.

The structure of a GEANT4 simulation can be described in terms of its class categories seen in Figure 4.1. The Global category is the basis of a GEANT4 simulation and handles random number generation, units and physical constants. The relevant classes for materials, particles and geometries are contained within their respective categories as well as in graphical representations. The Intercoms category handles communication between class levels

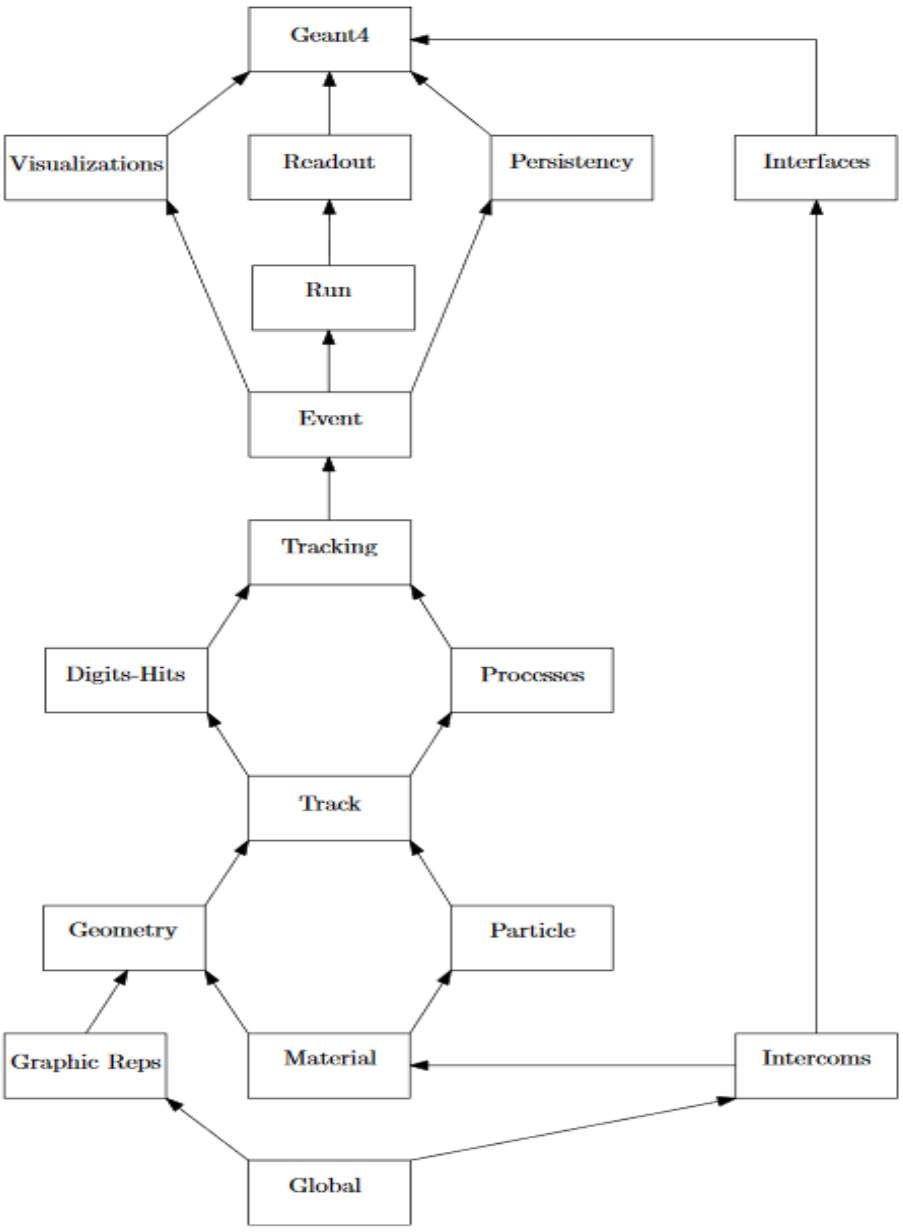

Figure 4.1: Flowchart describing the structure of a GEANT4 Simulation. Figure adopted from [10].

and categories. These classes allow the the program to create tracks which are broken down into processes and hits. Tracking uses these processes and hits to follow a particle moving through a volume. Events uses the classes in Tracking to manage tracks. Run then combines many events to create the final output of the simulation. An application developer's job is then to define the materials and geometry and to extract the relevant information out of a run, track or event.

The Livermore low energy physics package is one of the physics lists used in the application described here [30]. Its purpose is to handle electromagnetic physics for low energy particles and it was implemented in the hybrid detector application to handle ion passage physics in all materials. In the application, ions pass through a mylar window, an isobutane filled volume containing the ionization chamber, the Al dead layer of the DSSSD, and terminate in the Si of the DSSSD. Livermore handles the energy loss of ion tracks in each region and produces charges. Only the electron portion of the charge pairs are produced; the positive ions and electron holes are not. This is acceptable because at DRAGON the electron signal is read from the ionization chamber. The application then counts the number of electrons generated and multiplies them by the w value of isobutane (23 eV) [24] to estimate the measurable energy loss in the ionization chamber. For energy loss in the other regions the total loss calculated by the physics list is used. GEANT4 cannot handle electron drift so the application does not truly simulate an ionization chamber but it instead defines sensitive regions in the isobutane volume that collect event data. Figure 4.2 shows an example of an ion track entering the detector.

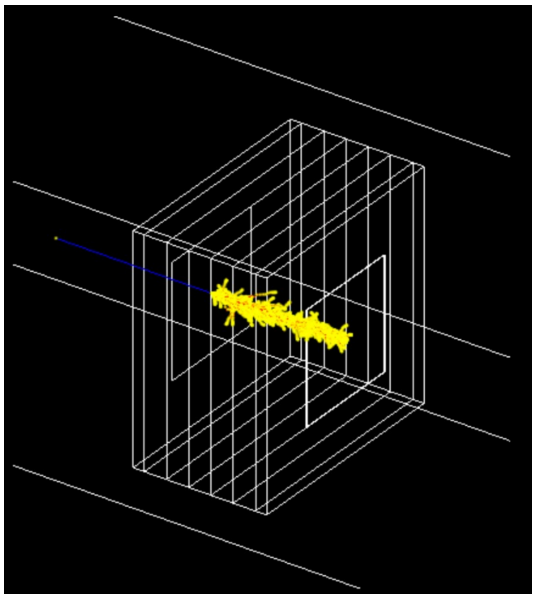

Figure 4.2: A single event of an ion passing through the detector. The path length is 6 cm. The volume is otherwise divided into five 1 cm wide sensitive regions with 0.5 cm separating the window from the ionization chamber and 0.5 cm separating the ionization chamber from the DSSSD. The blue line is the ion path, red lines are electron paths and yellow dots are hits. These are not the final dimensions of the hybrid detector.

The GEANT4 application was written to simulate the hybrid detector in order to determine the following design parameters:

1) The distance between the mylar window and the DSSSD. This is the *path length* of the detector.

2) The efficiency of the detector.

3) How the anodes comprising the ionization chamber should be electrically connected together.

In the simulation the DSSSD is a solid volume of Si with an Al dead layer so calculations here will not include losses from strip geometry or from the wire grid at either end of the ionization chamber. Here efficiency is defined as the

ratio of events terminating in Si to those which do not. Once the design was finalized the detector had to be capable of separating recoils from the beam and from isobaric contaminants in the dE vs E spectrum. To determine the above parameters nine test cases were considered. The test cases consisted of three reactions, which were ^{11}C(p,γ)^{12}N, ^{22}Ne(p,γ)^{23}Na, and ^{70}Kr(p,γ)^{71}Rb. Each reaction was investigated at three assumed beam energies: 150 keV/u, 1000 keV/u, and 1700 keV/u. These cases were selected because they include both the lightest and the heaviest cases likely to be tested at DRAGON as well as an intermediate mass case whose recoils are difficult to discriminate in the dE vs E spectrum.

4.2 Ionization Chamber Parameter Results

4.2.1 Path Length Determination

One parameter determined through simulation was the total distance between the entrance window and the surface of the DSSSD. We refer to this distance as the path length of the ions entering the detector. Selecting this length is important. The isobutane volume containing the detector can be operated as low as 4 torr stably so if the path length is very long then low energy ions will be stopped by the gas before they can terminate in the DSSSD. It may also be the case that instead of being terminated in the DSSSD they will instead terminate in the 0.4 μm thick aluminum dead layer of the DSSSD. If the detector is too short then we sacrifice the ionization chamber's ability to separate ions by Z and A. To select an appropriate length we considered a

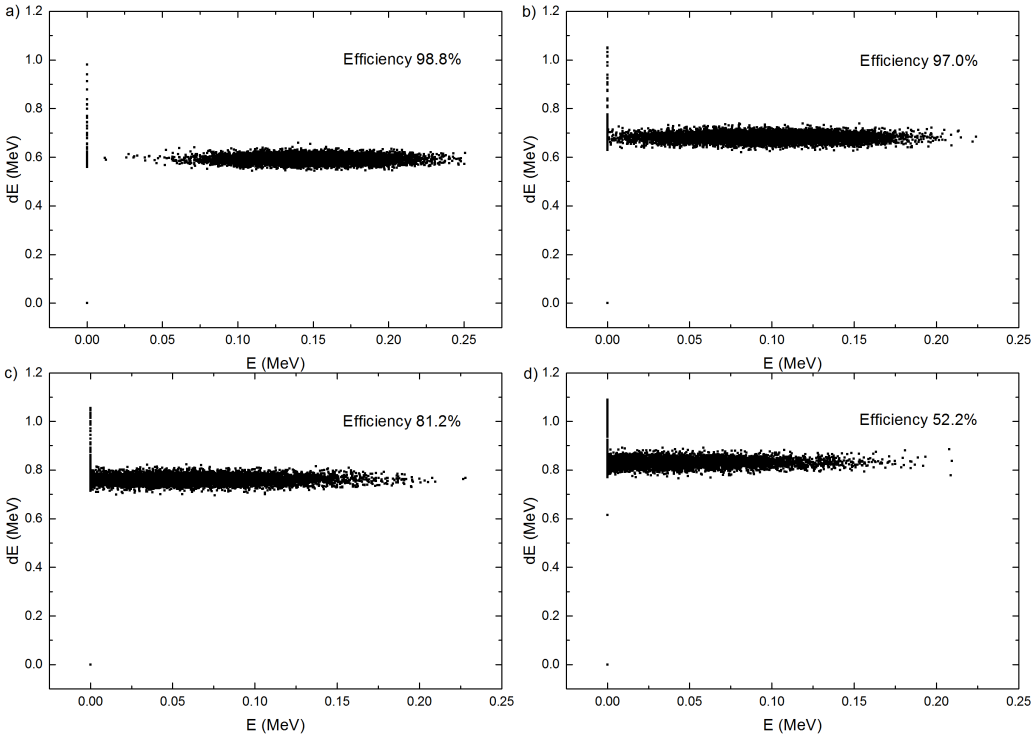

Figure 4.3: dE vs E spectra generated by simulation of the ^{11}C(p,γ)^{12}N reaction at beam energy 150 keV/u for path lengths a) 5 cm b) 6 cm c) 7 cm 8) 8 cm. Efficiency here is measured by the percentage of primary events which terminate in the sensitive volume of the DSSSD. The isobutane pressure was set to 4 torr, close to the lowest pressure we can confidently keep stable in the DRAGON system.

very light, very low energy reaction that we are likely to run at DRAGON. The ^{11}C(p,γ)^{12}N at 150 keV/u reaction products will be most easily stopped by 2 torr isobutane so we simulated the products and determined the efficiency of the detector with a 5, 6, 7, and 8 cm path length.

In Figure 4.3 we see that efficiency rapidly drops above a 6 cm path length. We had originally planned on a 6 cm path length for this reason but the ionization chamber must accommodate 1 cm of space for gaps between the window, ionization chamber and detector and 1 cm of insensitive anodes in

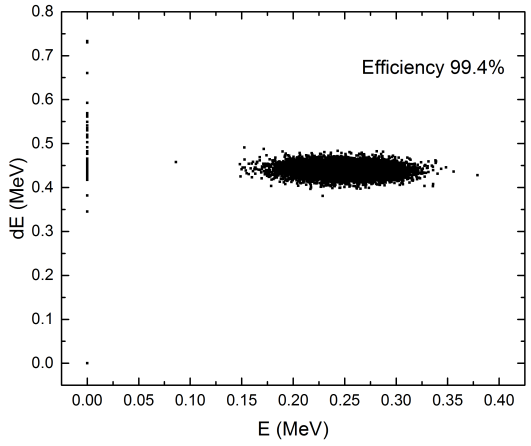

Figure 4.4: dE vs E spectrum generated by simulation of the $^{11}C(p,\gamma)^{12}N$ reaction at beam energy 150 keV/u for path length 7 cm operated at 2 torr of isobutane. At this path length and pressure we expect high efficiency, above 95%.

the ionization chamber. By adapting the gas system fittings on the end plate of the chamber we hope to be able to run confidently at 4 torr. By repeating the simulation at 2 torr in Figure 4.4 we expect that we can achieve high efficiency with a 7 cm path length.

4.2.2 Anode Configuration

Another parameter determinable through GEANT4 simulation is the configuration of the sensitive volume of the ionization chamber. The anodes can be soldered together to form a singular signal source. Figure 4.5 depicts the resolution of two possible configurations of the anodes.

The resolution improves as the signal producing regions increase in length. However Figure 4.6 demonstrates that the separation in stopping power curves tends to be greatest within the first few centimeters of isobutane at low ener-

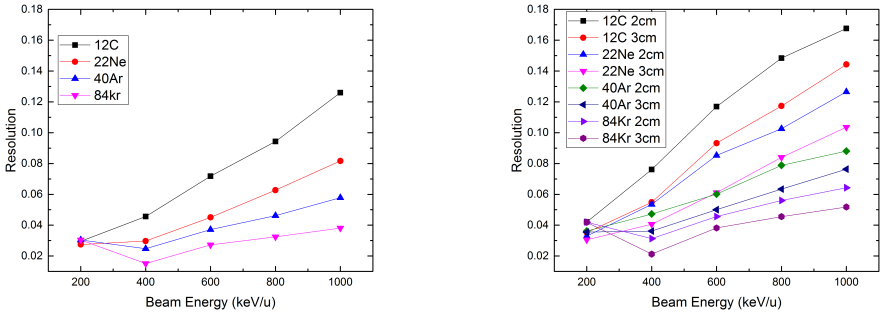

(a) One 5 cm long sensitive region. (b) A 2 cm and 3 cm long region.

Figure 4.5: The resolution of the ionization chamber for four ion species in 10 torr isobutane. Five 1 cm anodes soldered together have superior resolution to a configuration of 2 and 3 cm anodes.

gies. When operating at low energies the first two anodes and the last three anodes will be soldered together to better separate by Z, A, and energy loss. Unless otherwise specified, all energy loss data presented in this chapter was obtained by simulating a single 5 cm long sensitive region.

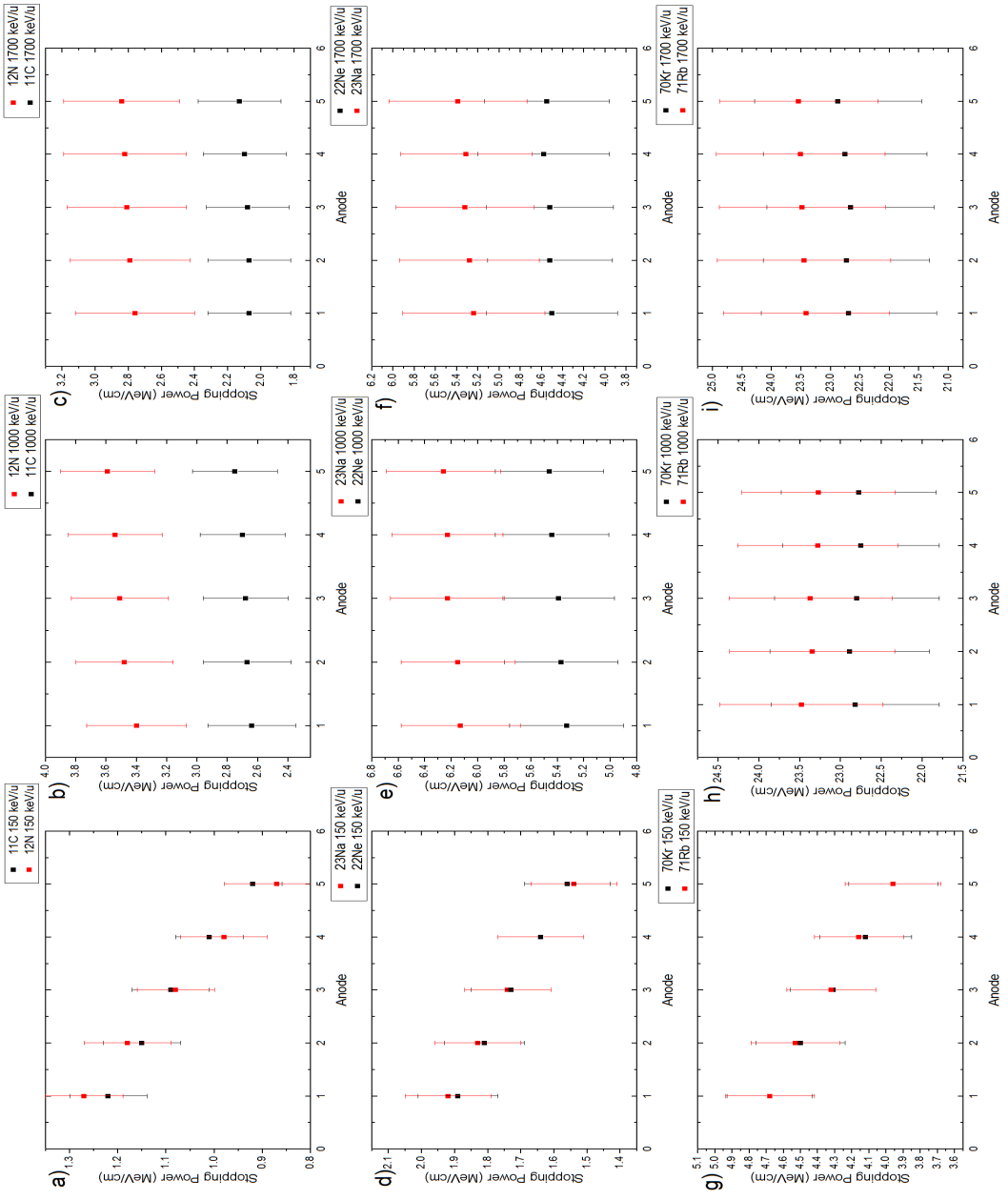
a)
b)
c)
d)
e)
f)
g)
h)
i)
11C 150 keV/u
12N 150 keV/u
12N 1000 keV/u
11C 1000 keV/u
12N 1700 keV/u
11C 1700 keV/u
23Na 150 keV/u
22Ne 150 keV/u
23Na 1000 keV/u
22Ne 1000 keV/u
22Ne 1700 keV/u
23Na 1700 keV/u
70Kr 150 keV/u
71Rb 150 keV/u
70Kr 1000 keV/u
71Rb 1000 keV/u
70Kr 1700 keV/u
71Rb 1700 keV/u
Stopping Power (MeV/cm)
Anode

Figure 4.6

Figure 4.6: Stopping powers read from each of five 1 cm long anode regions. Nine test cases were simulated. a), d), and g) are $^{11}C(p,\gamma)^{12}N$ at 150, 1000 and 1700 keV/u. b), e), and h) are $^{22}Ne(p,\gamma)^{23}Na$ at 150, 1000, 1700 keV/u. c), g), j) are $^{70}Kr(p,\gamma)^{71}Rb$ at 150, 1000, 1700 keV/u. In the 150 keV/u cases stopping power differences were greatest within the first 2 or 3 anodes. 150 keV/u cases were simulated in 4 torr isobutane and 1000 and 1700 keV/u cases were simulated in 10 torr isobutane.

4.3 Simulation Results Compared with Experiment

4.3.1 Comparing Stopping Powers with Experimental Data

Barbui *et al.* performed experiments to measure the energy loss of ^{40}Ar, ^{84}Kr, ^{197}Au and ^{238}U ions in mylar, Al and isobutane. They investigated four cases in isobutane which are compared against GEANT4 simulation results in Figure 4.7. For the cases of ^{197}Au, ^{84}Kr, and ^{238}U the GEANT4 simulation results are within 20% or less of the experimental values for most energies. Agreement worsens for all cases at low specific energies but agreement is especially poor for the case of ^{40}Ar. These comparisons demonstrate that precise calculations of stopping power and energy loss are unreliable for ions at low energies using the Livermore physics package in isobutane. Because of this, exact separation values calculated from simulation data should not be relied upon. Data presented here will represent qualitative differences with experiment as well as demonstrate separability of the recoil signal in dE vs E spectra.

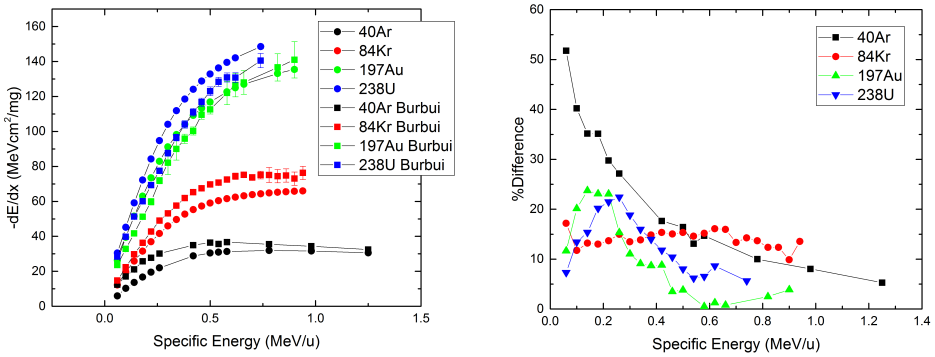

(a) Stopping Power. (b) Comparison with experiment.

Figure 4.7: Low energy stopping power comparisons for ions in isobutane. Simulation data is compared with experimental data from Barbui *et al.* [11].

4.3.2 Comparing Simulation to Real Spectra

In Figures 4.8 and 4.9 we compare simulation dE vs E spectra obtained with the hybrid detector to dE vs E spectra obtained with an ionization chamber. We demonstrate that the recoil signal can be separated from the beam and contaminants. In real spectra such as that seen in Figure 4.12 we observe a low energy tail in the dE vs E spectra. To account for this in simulation, primary event energy was sampled from an asymmetrical skewed Gaussian distribution over-top of a small constant energy background (see Figure 4.10). This energy profile for incoming events produced a low energy tail very similar to that observed in real experiments (see Figure 4.11). This suggests that the low energy tail seen in many recoil separators could be formed by a very small percentage of particles downscattering in energy due to collisions within the recoil separator such that their energy profile resembles a skewed distribution at energies between 0 and the distribution mean.

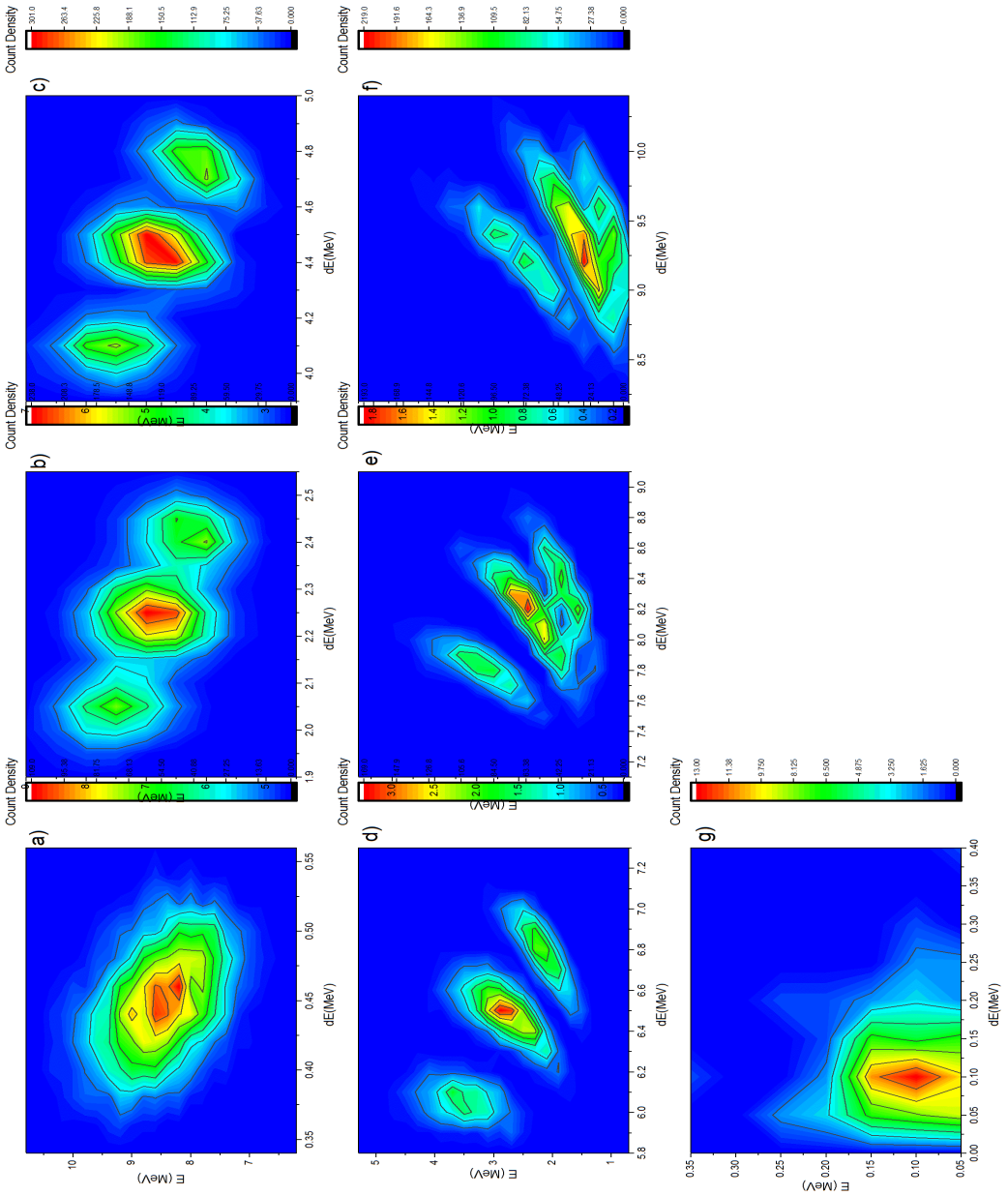

Figure 4.8

Figure 4.8: dE vs E spectra for the ^{23}Mg(p,γ)^{24}Al reaction with a ^{23}Na isobaric contaminant. ^{23}Mg events have energy 11.575 MeV, ^{24}Al events have energy 11.087 MeV, ^{23}Na events have energy 11.575 MeV, and ^{24}Mg events have 11.086 MeV. The leftmost and uppermost blob is the isobaric contaminant, the center is a mixture of magnesium isotopes and the lower and rightmost blob is the ^{24}Al recoil. a) through g) depict increasing pressure at 1, 5, 10, 15, 20, 25, and 30 torr respectively.

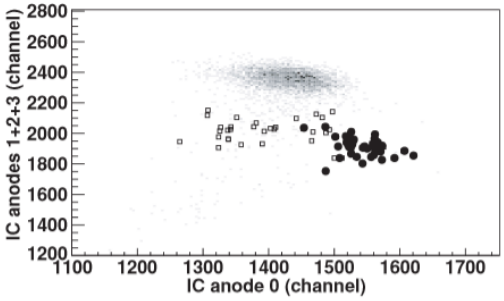

Figure 4.9: Experimental dE vs E spectrum obtained from the current ionization chamber for the ^{23}Mg(p,γ)^{24}Al reaction. The beam before hitting the gas target consisted of ^{23}Mg and ^{23}Na at 0.5032 MeV/u [12]. The gray density plot indicates the majority of counts with atomic mass 23, the empty squares are events with atomic mass 24 and the filled circles are the ^{24}Al recoil.

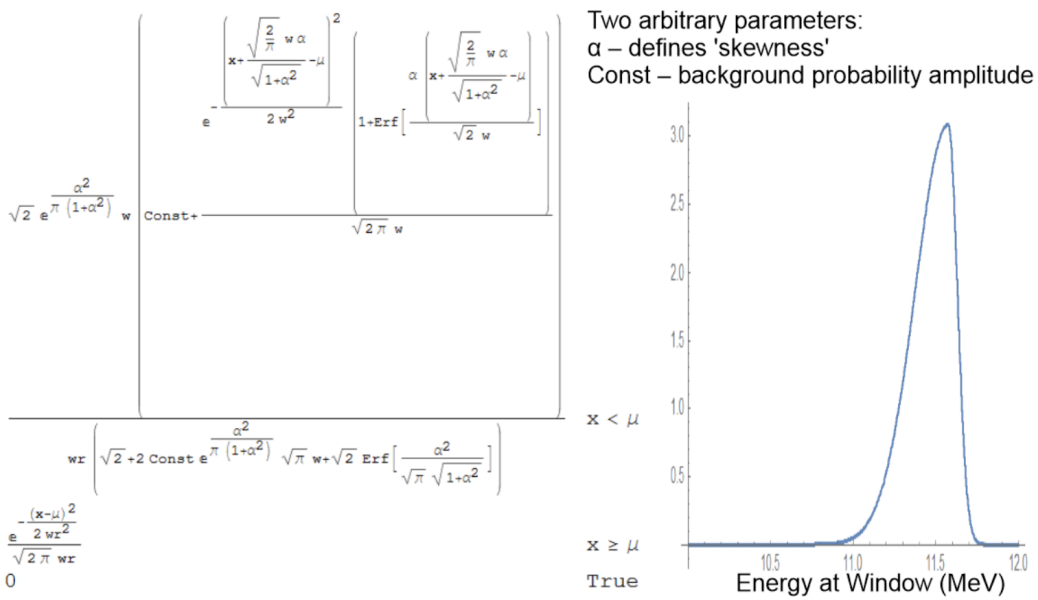

Figure 4.10: Sample energy distribution coded in Mathematica [13] that GEANT4 can sample energy values from. It is an asymmetrical skewed Gaussian distribution over-top of a small constant probability background.

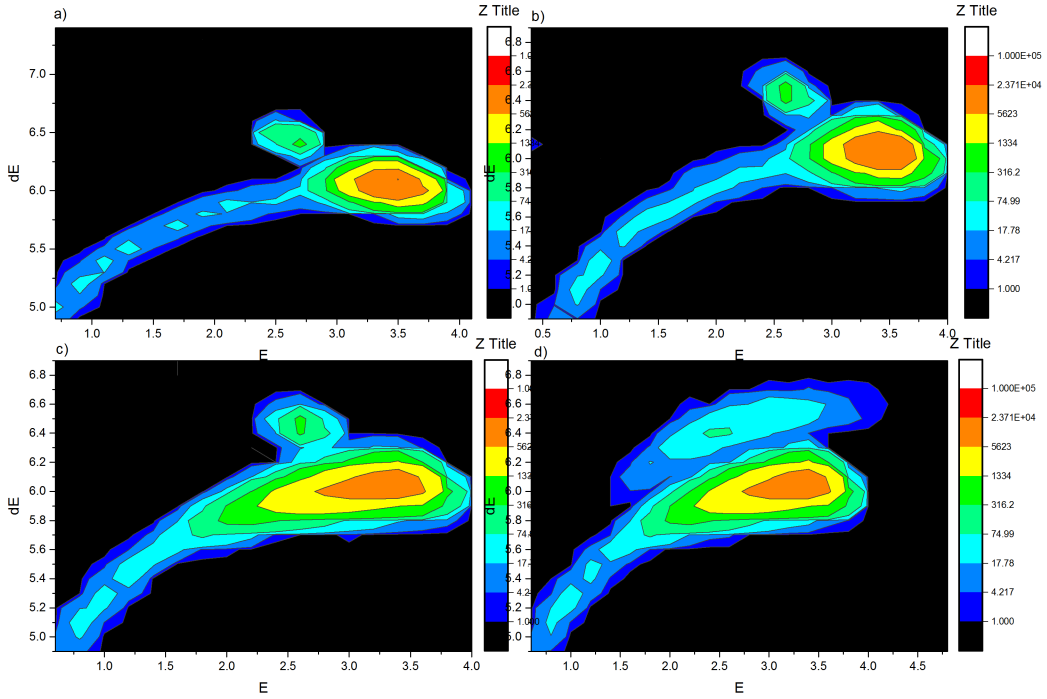

Figure 4.11: dE vs E spectra of ^{11}C and ^{12}N at 1000 keV/u with different ratios (R) of recoils to beam at the mean of the recoil energies. a) is $R = 0.001$, b) is $R = 0.002$, c) is $R = 0.01$ and d) is $R = 0.1$.

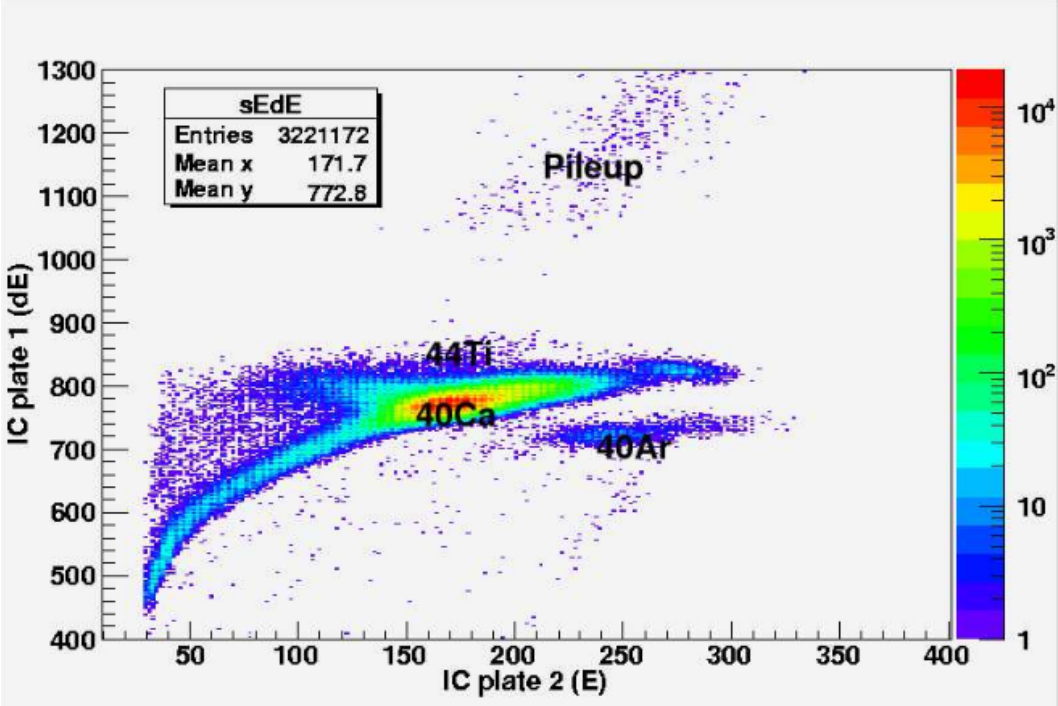

Figure 4.12: Experimental spectra for the ^{40}Ca(α,γ)^{44}Ti reaction. Shown is a typical run where the recoil peak is obscured by the leaky beam [14].

4.4 Final Design

The final parameters determined by simulation are 7 cm separating the 5 cm diameter circular entrance window from the DSSSD. Due to technical considerations this length was increased to 8.5 cm [15]; we still expect high efficiency (above 95%) is achievable for light, low energy cases provided the gas system can operate as low as 2 torr. The mylar window is 500 nm thick. 0.5 cm of space separates the ends of the ionization chamber from the window and the DSSSD. The ionization chamber will consist of five 1 cm wide anodes soldered together in a 2 cm and 3 cm configuration. On either end of the sensitive region are 1.0 cm wide anodes which are not read from due to irregularities in the electric field. An assembly and technical drawings can be seen in Appendix A.

Simulations suggest that the detector will be able to produce spectra with separable recoil signals even when considering a leaky beam. Originally the hybrid detector was intended to be housed in its own gas volume in an all new chamber. It will instead be suspended on an acrylic support inside the currently existing isobutane gas system at DRAGON. The acrylic support is fixed to an end plate designed to accommodate the electronics for the ionization chamber and the DSSSD as well as an expanded gas port to maintain 2 torr of pressure.

Chapter 5

Conclusions

5.1 Future Work

The hybrid detector will be most useful for light ions and low energy cases. An ideal test case would be a stable beam but a great first scientific application could be the $^{7}Be(\alpha,\gamma)^{11}C$ (experiment number S1692) reaction which recently received approval from the TRIUMF Experiment Evaluation Committee. For higher energy and heavier cases the 7 cm long ionization chamber can be swapped for the 25 cm ionization chamber currently in use at DRAGON. With technical drawings completed (see Appendix A) we hope to submit the design to the TRIUMF Design Group and have the detector manufactured and ready for testing on a stable beam by the beginning of January 2017.

5.2 Conclusions

In conclusion, a hybrid detector has been designed for use at DRAGON that will enhance the experimenters ability to discriminate recoils from beam particles at the end of the recoil separator. In combination with time-of-flight

measurements to suppress the leaky beam this detector should be capable of combining the strengths of both an ionization chamber and a DSSSD. This detector will allow experimenters to study reactions that have in the past been difficult to study due to the presence of isobaric contaminants.

Appendix A

(a) Isometric View

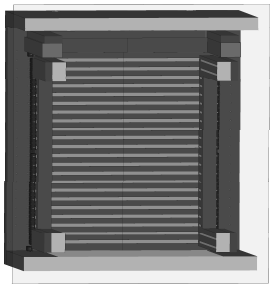

(b) Profile sectional view, rotated slightly.

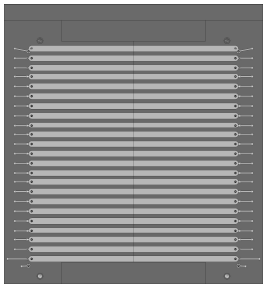

(c) Profile View

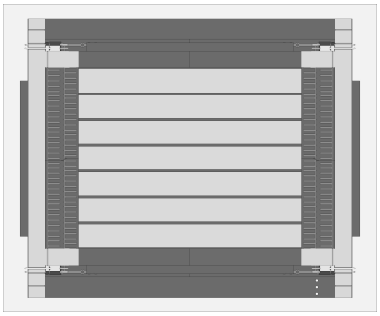

(d) Sectional Bottom View

Figure A.1: Assembly of the ionization chamber of the hybrid detector. Frisch grid wires are not shown here. The profile view is rotated slightly to better see the geometry [15].

Technical drawings for the ionization chamber portion of the hybrid detector are seen here. The author's designs were modified by Robert Henderson and the technical drawings were drawn by Irena Nikonov of the TRIUMF Detector Group [15].

Figure A.2: IC ANODE PCB

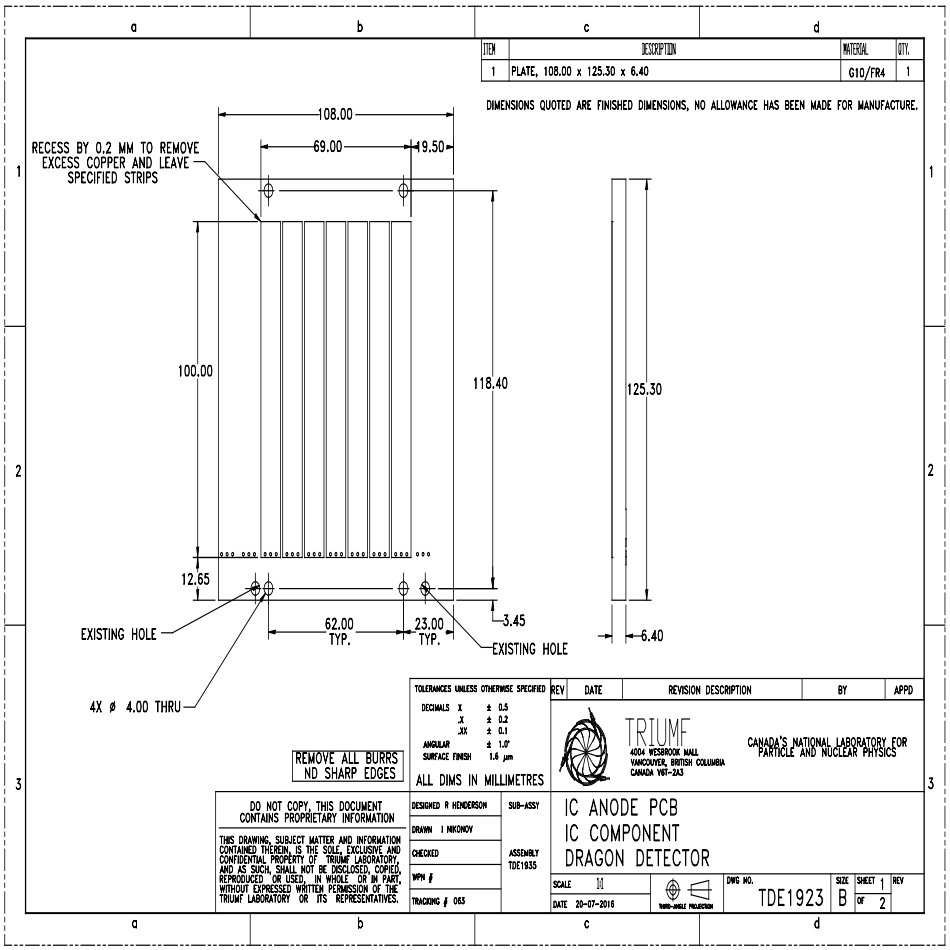

Figure A.3: IC END PCB

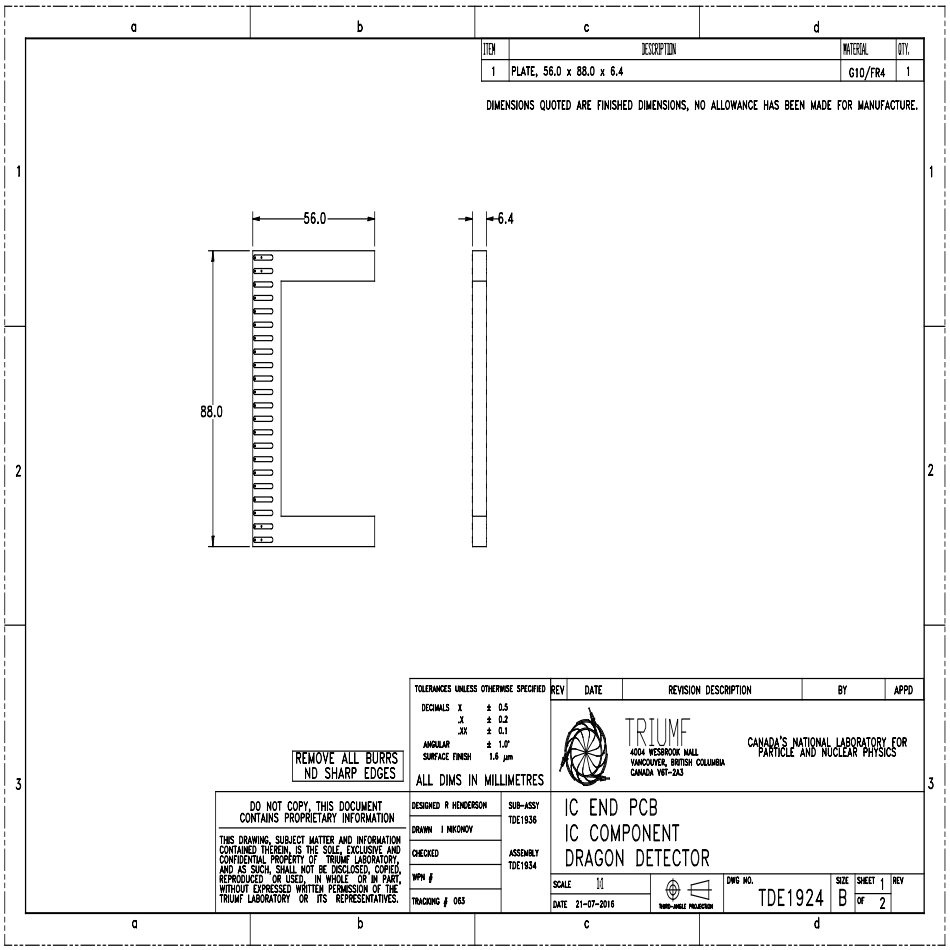

Figure A.4: IC END PCB STIFFENER

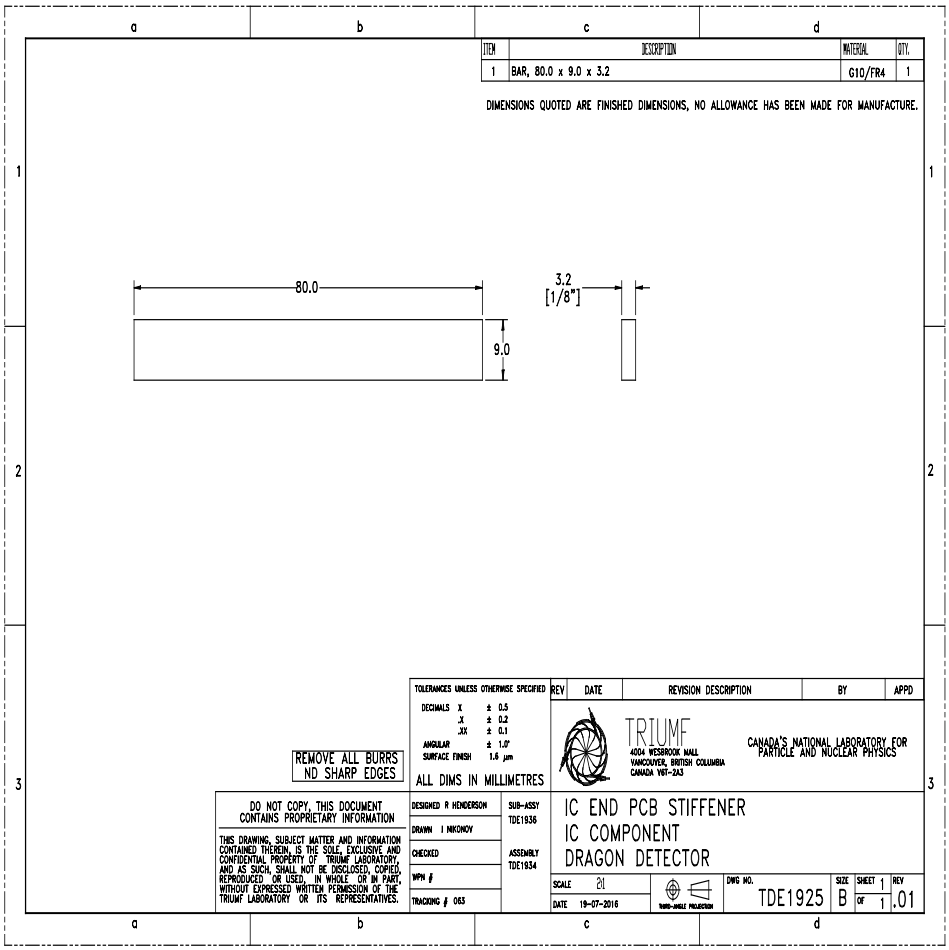

Figure A.5: IC CATHODE PCB

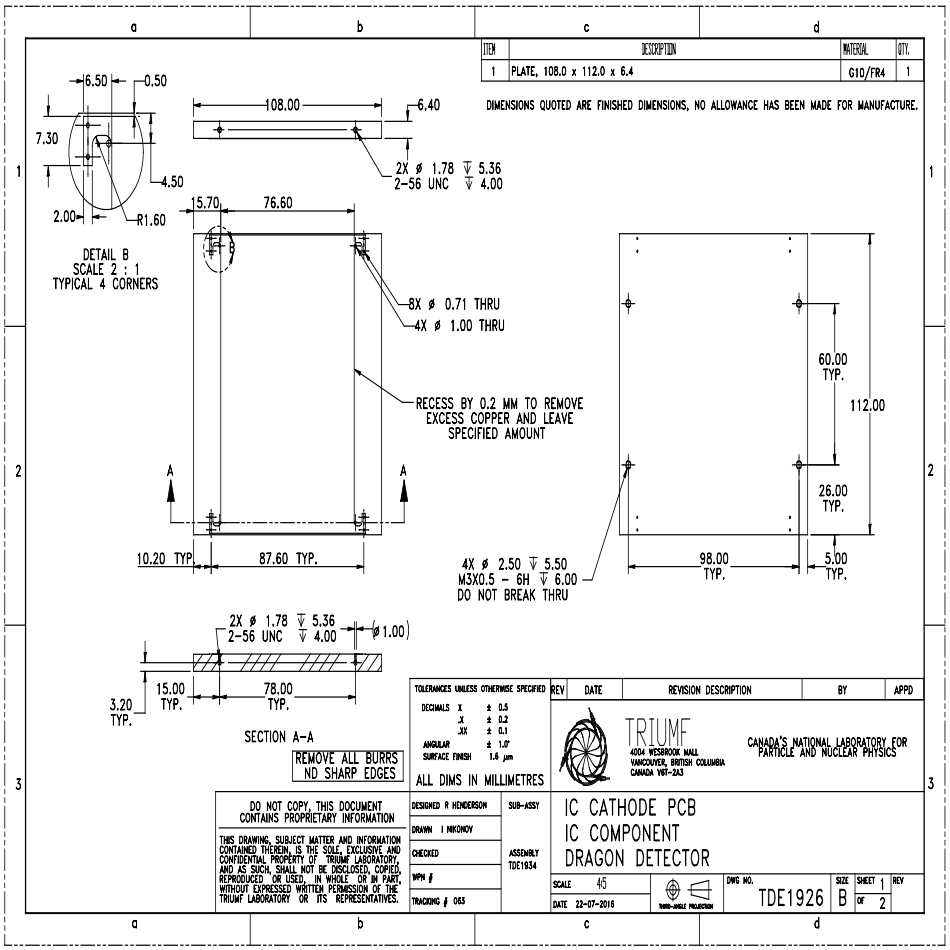

Figure A.6: IC FRISCH PCB STIFFENER

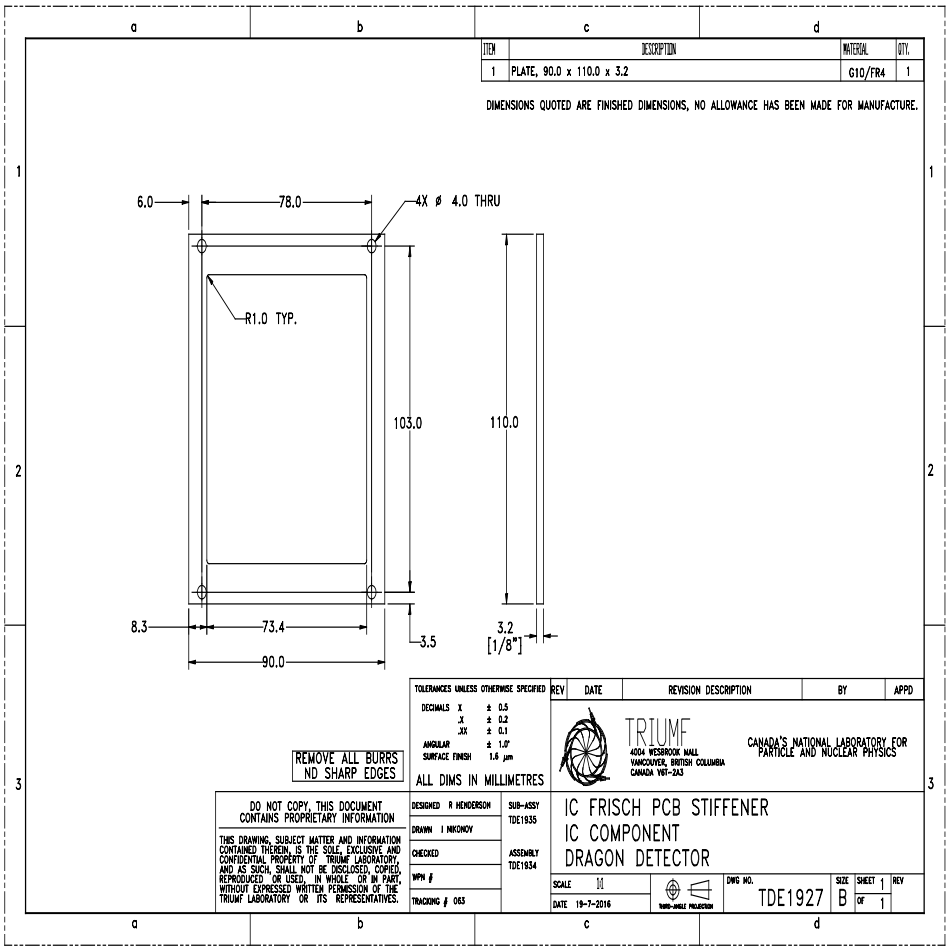

Figure A.7: IC FRISCH PCB TOP LEFT

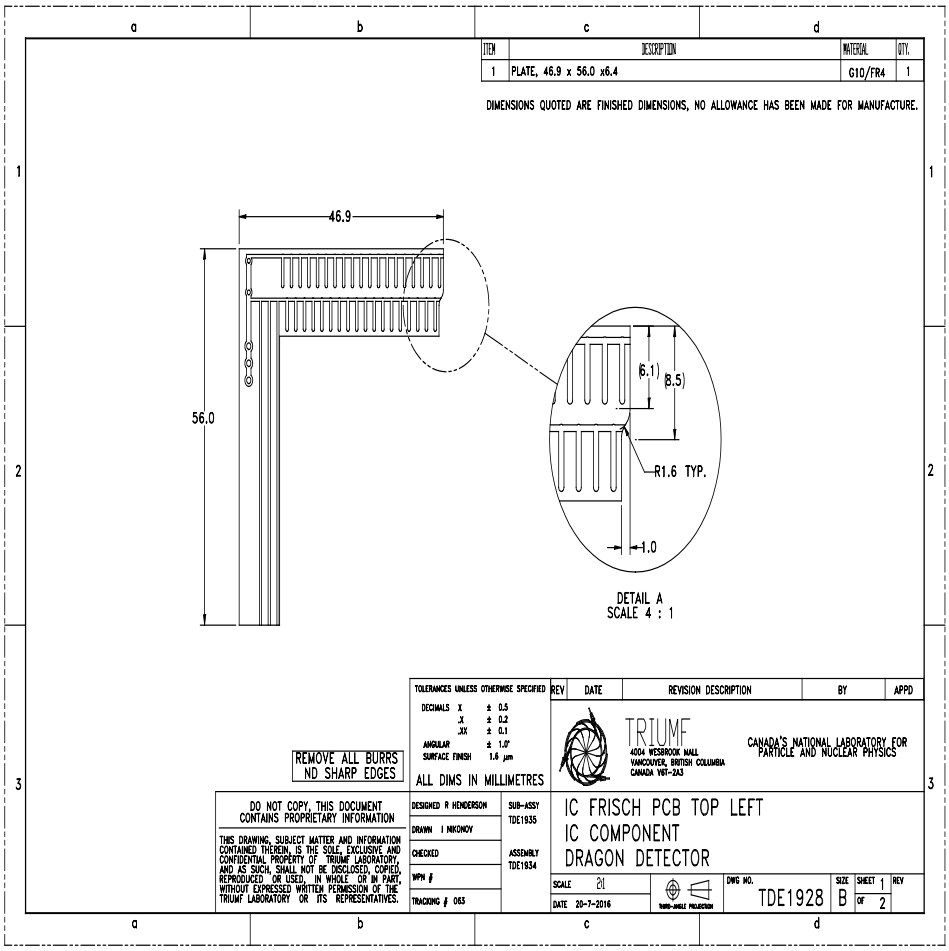

Figure A.8: IC FRISCH PCB TOP RIGHT

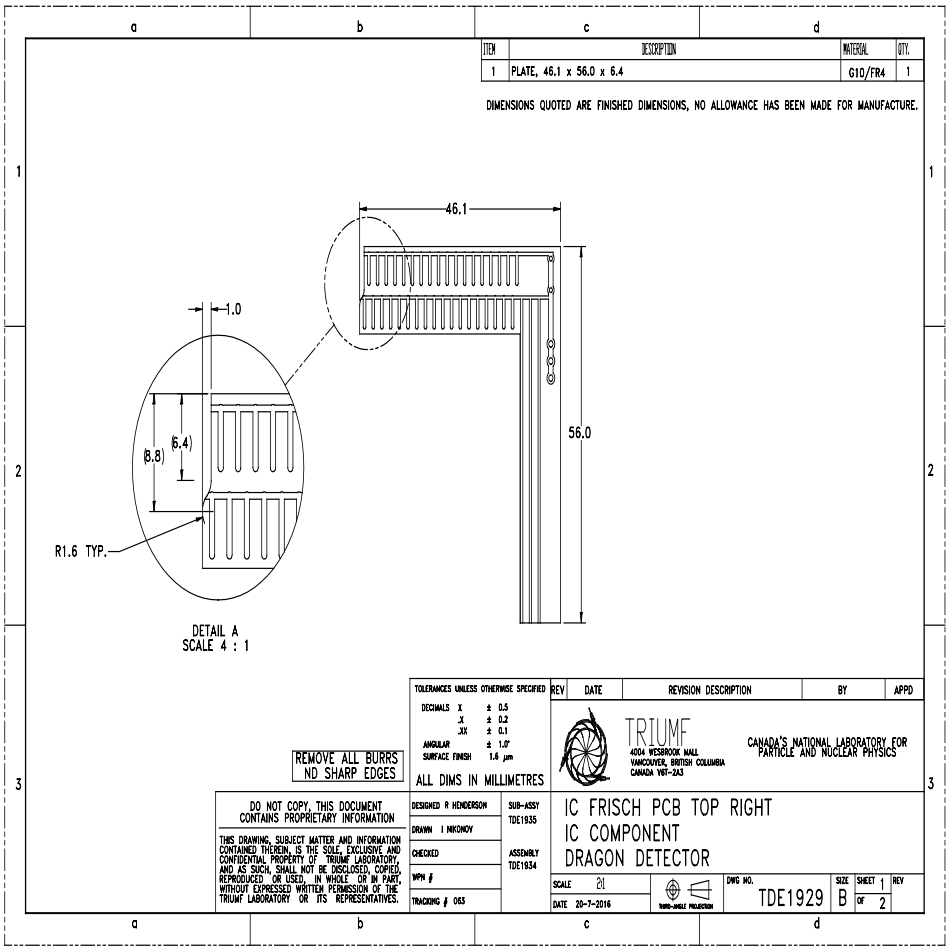

Figure A.9: IC SIDE PCB PART 1

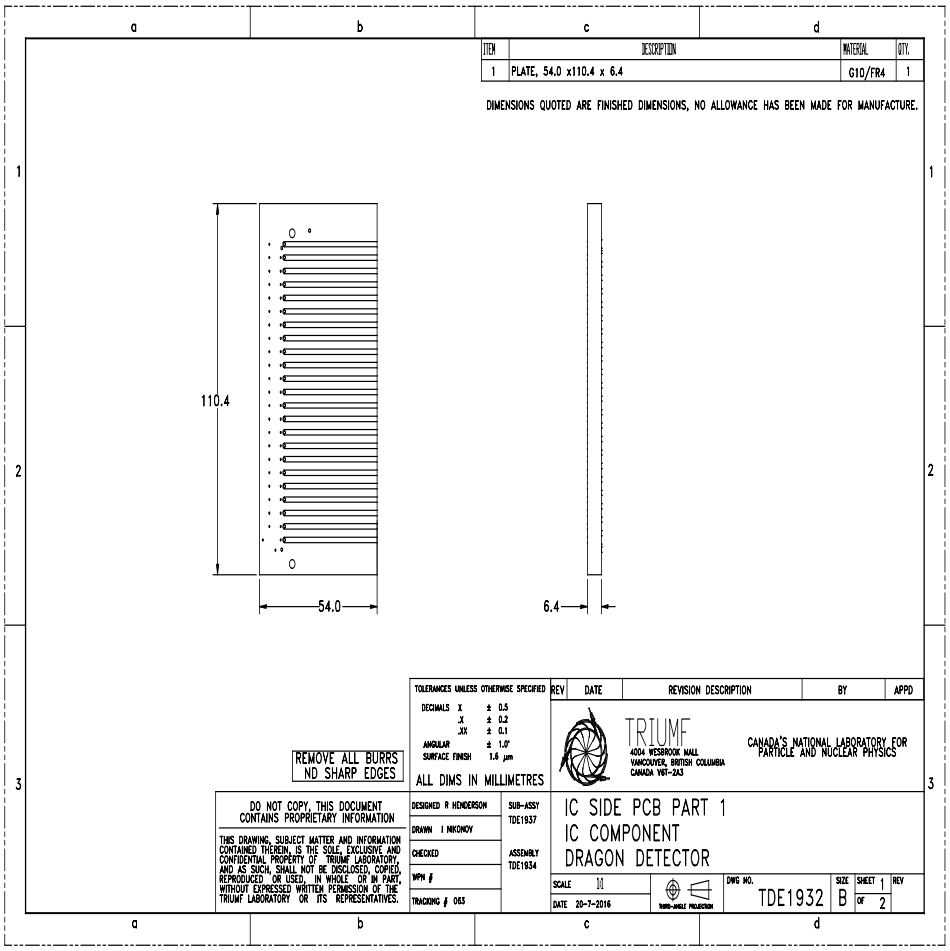

Figure A.10: IC SIDE PCB PART 2

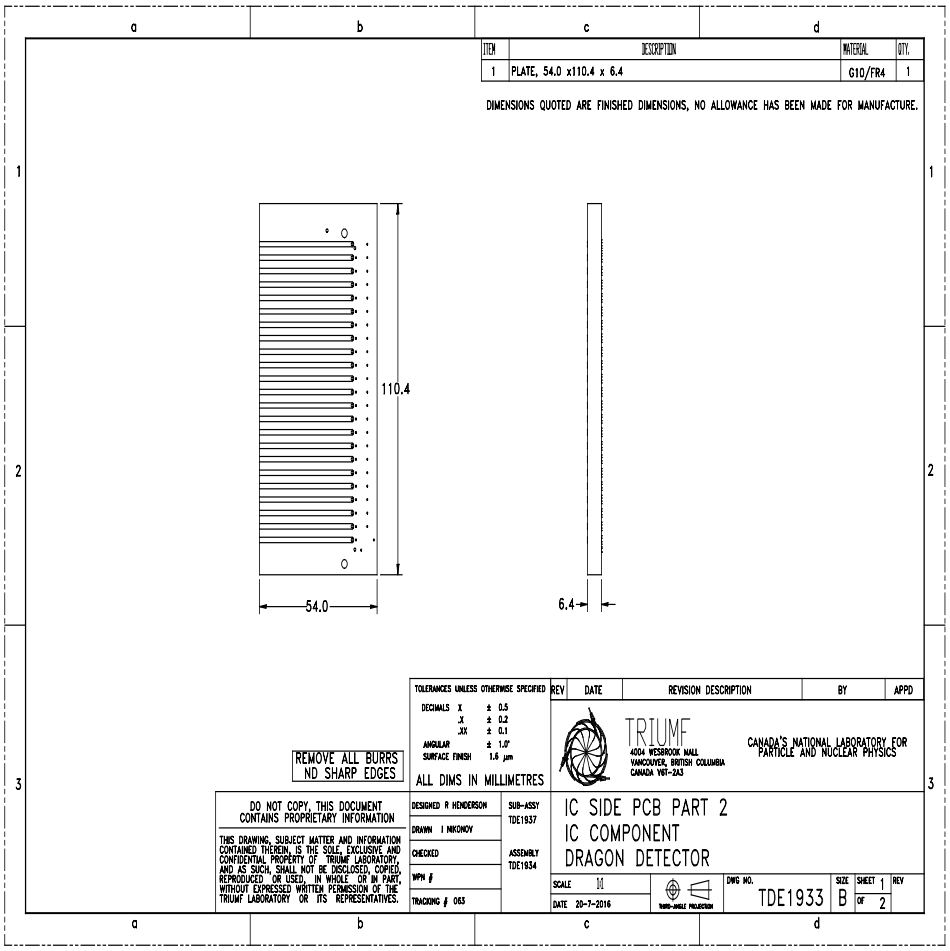

Figure A.11: IC SIDE PCB STIFFENER

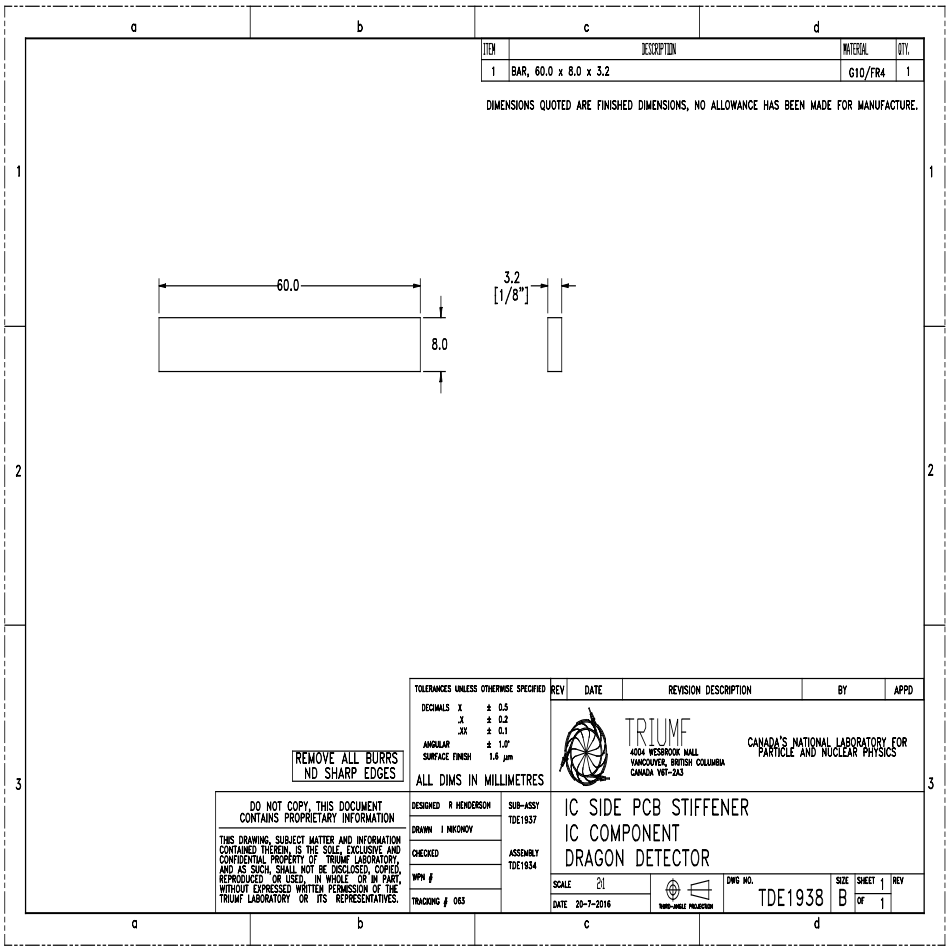

Bibliography

[1] AGW Cameron. Essays in nuclear astrophysics, ed. *C. Barnes, D. Clayton, and D.*

[2] Claus E Rolfs and William S Rodney. *Cauldrons in the cosmos: Nuclear astrophysics*. University of Chicago press, 1988.

[3] Christian Iliadis. *Nuclear Physics of Stars*. WILEY-VCH Verlag GmbH & Co. KGaA, 2007.

[4] DA Hutcheon, S Bishop, L Buchmann, ML Chatterjee, AA Chen, JM D'Auria, S Engel, D Gigliotti, U Greife, D Hunter, et al. The dragon facility for nuclear astrophysics at triumf-isac: design, construction and operation. *Nuclear Instruments and Methods in Physics Research Section A: Accelerators, Spectrometers, Detectors and Associated Equipment*, 498(1):190–210, 2003.

[5] Michael Joseph Lamey. *A microchannel detection system for DRAGON*. PhD thesis, Simon Fraser University, 2004.

[6] Glenn F Knoll. *Radiation detection and measurement*. John Wiley & Sons, 2010.

[7] Shawn Bishop. *Direct Measurement of the 21Na (p, y) 22Mg Resonant Reaction Rate in Nova Nucleosynthesis*. PhD thesis, Department of Physics-Simon Fraser University, 2003.

[8] William R Leo. *Techniques for nuclear and particle physics experiments: a how-to approach*. Springer Science & Business Media, 2012.

[9] Robley Dunglison Evans and Atome Noyau. *The atomic nucleus*, volume 582. McGraw-Hill New York, 1955.

[10] Geant Collaboration. Introduction to geant4. 2010.

[11] M Barbui, D Fabris, M Lunardon, S Moretto, G Nebbia, S Pesente, G Viesti, M Cinausero, G Prete, V Rizzi, et al. Energy loss of energetic 40 ar, 84 kr, 197 au and 238 u ions in mylar, aluminum and isobutane. *Nuclear Instruments and Methods in Physics Research Section B: Beam Interactions with Materials and Atoms*, 268(1):20–27, 2010.

[12] L Erikson, C Ruiz, F Ames, P Bricault, L Buchmann, AA Chen, J Chen, H Dare, B Davids, C Davis, et al. First direct measurement of the mg 23 (p, γ) al 24 reaction. *Physical Review C*, 81(4):045808, 2010.

[13] Wolfram Research, Inc. Mathematica 11, 2015.

[14] Christian Ouellet. *The 40Ca (α, γ) 44Ti Nuclear Reaction Using DRAGON*. PhD thesis, McMaster University, 2007.

[15] R Henderson and I Nikonov. Triumf detector group, 2016.

[16] George Gamow et al. The evolution of the universe. *Nature*, 162(4122):680–682, 1948.

[17] Hans E Suess and Harold C Urey. Abundances of the elements. *Reviews of Modern Physics*, 28(1):53, 1956.

[18] E Margaret Burbidge, Geoffrey Ronald Burbidge, William A Fowler, and Fred Hoyle. Synthesis of the elements in stars. *Reviews of modern physics*, 29(4):547, 1957.

[19] SE Woosley and WM Howard. The p-process in supernovae. *The Astrophysical Journal Supplement Series*, 36:285–304, 1978.

[20] H Schatz, A Aprahamian, J Görres, M Wiescher, T Rauscher, JF Rembges, F-K Thielemann, B Pfeiffer, P Möller, K-L Kratz, et al. rp-process nucleosynthesis at extreme temperature and density conditions. *Physics reports*, 294(4):167–263, 1998.

[21] S Bishop, RE Azuma, L Buchmann, AA Chen, ML Chatterjee, JM D'Auria, S Engel, D Gigliotti, U Greife, M Hernanz, et al. N a 21 (p, γ) m g 22 reaction and oxygen-neon novae. *Physical review letters*, 90(16):162501, 2003.

[22] Quantar technologies inc., 1999.

[23] NR Campbell and VJ Francis. A theory of valve and circuit noise. *Electrical Engineers-Part III: Radio and Communication Engineering, Journal of the Institution of*, 93(21):45–52, 1946.

[24] I Krajcar Bronic. A study of argon-isobutane mixtures in a proportional counter: gas amplification, w value, and energy resolution. *Radiation Protection Dosimetry*, 61(1-3):263–266, 1995.

[25] ICRU. Average energy required to produce an ion pair (report 31). 1979.

[26] JW Mayer, G Bertolini, and A Coche. Semiconductor detectors. *North-Holland Publ. Co, Amsterdam*, 1968.

[27] Chris Wrede, Ahmed Hussein, Joel G Rogers, and John D'Auria. A double sided silicon strip detector as a dragon end detector. *Nuclear Instruments and Methods in Physics Research Section B: Beam Interactions with Materials and Atoms*, 204:619–624, 2003.

[28] Oskar Klein and Yoshio Nishina. Über die streuung von strahlung durch freie elektronen nach der neuen relativistischen quantendynamik von dirac. *Zeitschrift für Physik*, 52(11-12):853–868, 1929.

[29] Sea Agostinelli, John Allison, K al Amako, J Apostolakis, H Araujo, P Arce, M Asai, D Axen, S Banerjee, G Barrand, et al. Geant4—a simulation toolkit. *Nuclear instruments and methods in physics research section A: Accelerators, Spectrometers, Detectors and Associated Equipment*, 506(3):250–303, 2003.

[30] D Wright et al. Geant4 physics reference manual. Technical report, Tech. Rep.(Geant4 Collaboration, 2006), 2007.